

**Gas/Solids Mass Flow Measurement by  
Electrical Capacitance Tomography and  
Electrostatic Sensors**

**A THESIS SUBMITTED TO THE UNIVERSITY OF MANCHESTER  
FOR THE DEGREE OF MASTER OF PHILOSOPHY  
IN THE FACULTY OF SCIENCE AND ENGINEERING**

**2018**

**KHURSI AH ZAINAL MOKHTAR**

**SCHOOL OF ELECTRICAL AND ELECTRONIC ENGINEERING**

# Table of Contents

List of Figures .....	14
List of Tables .....	6
List of Abbreviations .....	7
List of Symbols .....	8
Abstract .....	10
Declaration .....	11
Copyright Statement .....	12
Publication from this work.....	13
Acknowledgement .....	14
CHAPTER 1: INTRODUCTION .....	15
1.1 Background .....	15
1.2 Problem and Motivation .....	16
1.3 Research Objectives.....	16
1.4 Thesis Outline .....	17
CHAPTER 2: LITERATURE REVIEW .....	18
2.1 Electrostatic Sensor.....	18
2.2 Electrical Capacitance Tomography (ECT).....	20
2.2.1 Mathematical Formulation of the Sensor Model .....	21
2.2.2 General Principles of ECT Measurement .....	23
2.2.3 ECT Sensor and Normalisation of Capacitance Measurement.....	24
2.2.4 Sensitivity Matrix .....	26
2.2.5 Image Reconstruction Algorithms .....	26
2.3 Principle of Mass Flow Measurement .....	29
2.3.1 Velocity Measurement and Cross-correlation Technique.....	30
2.3.2 Particle Concentration Measurement.....	32
CHAPTER 3: EXPERIMENTAL SETUP AND INSTRUMENTATION.....	34

3.1 Designed of Mass Flow Meter by ECT and Electrostatic Sensor .....	34
3.2 ECT Sensor Model.....	35
3.2.1 Sensitivity Matrix Generation.....	37
3.2.2 ECT Image Reconstruction.....	40
3.3 Electrostatic Sensor System .....	41
3.3.1 Electrostatic Sensing Head .....	41
3.3.2 Signal Conditioning Circuit.....	44
3.3.3 Data Acquisition System .....	45
3.4 Mass Flow Measurement on Standpipe .....	46
3.4.1 Pilot-plant Scale CFB .....	47
3.4.2 Experimental Setup.....	47
3.5 Mass Flow Measurement on Gravity Flow Rig .....	49
3.5.1 Optimising Electrode Length and Distance of Electrostatic Sensor .....	49
3.5.2 Assessing the Performance of Optimised Electrode Length and Distance.....	50
3.5.3 Mass Flow Meter by ECT and Two Sets of Electrostatic Sensor.....	51
3.5.4 Solids Velocity Using Two Sets of Electrostatic Sensor.....	52
3.5.5 Mass Flow Calculation and Assessing the Performance of Mass Flow Meter .....	53
CHAPTER 4: RESULTS AND DISCUSSION .....	55
4.1 Electrostatic Sensor on Standpipe.....	55
4.2 ECT Images of Gas/Solid Flow in a Standpipe .....	58
4.3 Optimised Electrode Length and Distance.....	62
4.4 Solids Velocity Measurement Using Two Sets of Electrostatic Sensor.....	66
4.5 Mass Flow Calculation and Performance Analysis of Mass Flow Meter .....	67
CHAPTER 5: CONCLUSIONS AND SUGGESTION FOR FUTURE WORK .....	70
5.1 Conclusions.....	70
5.2 Suggestion for Future Works .....	71
REFERENCES .....	72

## List of Figures

		<b>Page</b>
Figure 2.1	An electrostatic sensor system	18
Figure 2.2	Subsystem of cross-correlation flow meter	19
Figure 2.3	An ECT system	21
Figure 2.4	ECT sensor	25
Figure 2.5	Schematic diagram of ECT sensor cross-section	25
Figure 2.6	Flowchart of LBP image reconstruction algorithm	28
Figure 2.7	Velocity measurement using the cross-correlation technique	30
Figure 2.8	Schematic diagram of rope formed by flow through a bend	33
Figure 3.1	Mass flow measurement system for CFB	34
Figure 3.2	Mass flow measurement system for gravity flow rig	35
Figure 3.3	ECT sensor model used for mass flow measurement on standpipe and gravity flow rig	35
Figure 3.4	(a) 2D schematic diagram of 12-electrode ECT sensor drawn using COMSOL, and (b) FE meshing	38
Figure 3.5	Sensitivity maps for 8-electrode ECT sensor	39
Figure 3.6	Sensitivity maps for 12-electrode ECT sensor	40
Figure 3.7	Cross-sectional views with descriptions of (a) insulated and (b) exposed ring-shaped electrodes	42
Figure 3.8	Photo of the sensing head	42
Figure 3.9	Cross-sectional view of the structure of the sensing head	43
Figure 3.10	(a) Electrostatic sensing head with shielding on gravity flow rig, and (b) the circular-ring shaped electrode of the electrostatic sensor	44
Figure 3.11	Schematic diagram of a signal conditioning circuit	45
Figure 3.12	Block diagram of a DAQ system for electrostatic sensor	46
Figure 3.13	Schematic diagram of the test facility of circulating fluidised bed (CFB)	48
Figure 3.14	Schematic diagram of gravity flow rig used to investigate the optimisation of electrode length and distance between upstream and	50

	downstream electrodes, (b) the cross-sectional area of the gravity flow rig and (c) the circular-ring shaped electrode of the electrostatic sensor	
Figure 3.15	Schematic diagram of an ECT sensor and two sets of electrostatic sensor attached on gravity flow rig	52
Figure 3.16	Gravity flow rig with an ECT sensor and two sets of electrostatic sensor	53
Figure 4.1	Output signals from upstream and downstream electrodes for dry sand at fluidisation velocity of (a) $2 \text{ m s}^{-1}$ , (b) $4 \text{ m s}^{-1}$ , (c) $6 \text{ m s}^{-1}$ , (d) $8 \text{ m s}^{-1}$ and (e) $10 \text{ m s}^{-1}$	56
Figure 4.2	Output signals from upstream and downstream electrodes for dry granule corn at fluidisation velocity of (a) $2 \text{ m s}^{-1}$ , (b) $4 \text{ m s}^{-1}$ , (c) $6 \text{ m s}^{-1}$ , (d) $8 \text{ m s}^{-1}$ and (e) $10 \text{ m s}^{-1}$	57
Figure 4.3	Experimental result from sub-section 3.5 conducted using electrostatic sensor with electrode length of 2 mm and distance of 2 cm.	58
Figure 4.4	(a) Signals from upstream and downstream electrodes and (b) Cross-correlation curve for ring-shaped electrode with length of 2 mm and distance of 2 cm	62
Figure 4.5	(a) Signals from upstream and downstream electrodes and (b) Cross-correlation curve for ring-shaped electrode with length of 2 mm and distance of 4 cm	62
Figure 4.6	(a) Signals from upstream and downstream electrodes and (b) Cross-correlation curve for ring-shaped electrode with length of 2 mm and distance of 6 cm	63
Figure 4.7	(a) Signals from upstream and downstream electrodes and (b) Cross-correlation curve for ring-shaped electrode with length of 2 mm and distance of 8 cm	63
Figure 4.8	(a) Signals from upstream and downstream electrodes and (b) Cross-correlation curve for ring-shaped electrode with length of 2 mm and distance of 10 cm	64

## List of Tables

		<b>Page</b>
Table 2.1	Capacitance measurements produced from pairs of excited and other electrodes	24
Table 3.1	Physical ECT sensor parameters	37
Table 3.2	Material densities and dielectric constants for sand and corn	48
Table 3.3	Height (in m) from the opening of the gravity flow rig to the centre of electrostatic sensor	51
Table 4.1	ECT images of gas/solids flow for dry sand in a standpipe with five different fluidisation velocities	60
Table 4.2	ECT images of gas/solids flow for dry granule corn in a standpipe with five different fluidisation velocities	61
Table 4.3	Experimental results of ring-shaped electrode with length of 2 mm and various distances	64
Table 4.4	Experimental results of ring-shaped electrode with length of 4 mm and various distances	64
Table 4.5	Experimental results of ring-shaped electrode with length of 6 mm and various distances	65
Table 4.6	Experimental results of ring-shaped electrode with length of 8 mm and various distances	65
Table 4.7	Experimental results of ring-shaped electrode with length of 10 mm and various distances	65
Table 4.8	Free fall velocity (in $\text{m s}^{-1}$ ) for various electrode lengths and various distances between up-stream and down-stream electrode	65
Table 4.9	Absolute error (%) for various electrode length and various distances between up-stream and down-stream electrodes	66
Table 4.10	Experimental results of two sets of electrostatic sensor, ES1 and ES2, and correlation velocity at ECT section	66
Table 4.11	Mean concentration of salt in gravity flow rig for all measurements	67
Table 4.12	ECT images for gas/solids flow of salt in gravity flow rig at $t=4\text{s}$ until $t=12\text{s}$ with 4s interval	68
Table 4.13	Measured mass, reference mass and absolute error for all measurements	69

## List of Abbreviations

<b>CT</b>	Computerised Tomography
<b>DAS</b>	Data Acquisition System
<b>ECT</b>	Electrical Capacitance Tomography
<b>PT</b>	Process Tomography
<b>CFB</b>	Circulating Fluidised Bed
<b>LBP</b>	Linear Back Projection
<b>NI</b>	National Instrument
<b>NOx</b>	Nitrogen Oxides
<b>ES1</b>	Upper electrostatic sensor
<b>ES2</b>	Lower electrostatic sensor

## List of Symbols

$A$	Cross-sectional area of electrodes
$\varepsilon_0$	Permittivity of free space
$d$	Distance between ECT electrode
$\varepsilon_r$	Relative permittivity
$D$	Electric displacement field
$\rho_f$	Free charge density
$E$	Electric field
$\phi$	Electrical Potential
$i$	Source electrode
$j$	Detecting electrode
$\Gamma$	Surface of electrode
$Q$	Charge
$V$	Voltage
$N$	Number of electrodes
$C$	Capacitance value
$M$	Number of capacitance measurements
$\lambda$	Normalised capacitance
$p$	Pixel element
$S$	Sensitivity value
$\hat{g}$	Grey level
$\eta$	Threshold level
AVG	Average operator
$R$	Cross-correlation function
$x$	Signal from upstream electrode
$y$	Signal from downstream electrode
$T$	Integral time



$\tau$	Time delay
$v$	Velocity
$m$	Mass
$k$	Number of pixels
$L$	Electrode length
$d$	Distance between upstream and downstream electrodes
$g$	Acceleration due to gravity
$H$	Height

## Abstract

Solids velocity, solids concentration and mass of solids are important parameters describing the flow state of gas/solids two-phase systems. In this work, two mass flow measurement systems built based on ECT and electrostatic sensor. One mass flow meter built on a standpipe of circulating fluidised bed (CFB) is based on an ECT sensor and an electrostatic sensor. Another mass flow meter built on a gravity flow rig is based on an ECT sensor and two sets of electrostatic sensor. The two sets of electrostatic sensor mounted at each end of the ECT sensor are built to deal with velocity before and after ECT sensor. The construction of the two sets of electrostatic sensor on a gravity flow rig involved searching for optimised electrode length and distance between upstream and downstream electrodes of electrostatic sensor. The optimised electrode length and distance are chosen based on the least absolute error which calculated based upon correlation velocity and free fall velocity. The outputs of electrostatic sensor built on the standpipe had been swamped by noise and determining the solid velocity using cross-correlation technique is rather impossible. Meanwhile, ECT sensor gives images of gas/solids flow in standpipe that show stable flows for dry sand for fluidisation velocity of  $2 \text{ m s}^{-1}$  until  $8 \text{ m s}^{-1}$  and unstable flow for fluidisation of  $10 \text{ m s}^{-1}$ . For granule corn, the ECT images show stable flows for fluidisation velocity of  $2 \text{ m s}^{-1}$ ,  $4 \text{ m s}^{-1}$  and  $10 \text{ m s}^{-1}$  whereas at fluidisation velocity of  $6 \text{ m s}^{-1}$  and  $8 \text{ m s}^{-1}$  unstable flows shown in ECT images. The developed mass flow meter based on an ECT sensor and two sets of electrostatic sensor gives absolute error of 0.75%, 0.47%, 0.33% and 1.22% for first, second, third and fourth measurements, respectively. It gives satisfactory results as all the absolute error values are below 2%. This satisfactory results reveal that it is feasible to develop the mass flow meter based on an ECT sensor and two sets of electrostatic sensor.

## **Declaration**

No portion of the work referred to in the thesis has been submitted in support of an application for another degree or qualification of this or any other university or other institute of learning.

## Copyright Statement

i. The author of this thesis (including any appendices and/or schedules to this thesis) owns certain copyright or related rights in it (the “Copyright”) and s/he has given The University of Manchester certain rights to use such Copyright, including for administrative purposes.

ii. Copies of this thesis, either in full or in extracts and whether in hard or electronic copy, may be made only in accordance with the Copyright, Designs and Patents Act 1988 (as amended) and regulations issued under it or, where appropriate, in accordance Presentation of Theses Policy You are required to submit your thesis electronically Page 11 of 25 with licensing agreements which the University has from time to time. This page must form part of any such copies made.

iii. The ownership of certain Copyright, patents, designs, trademarks and other intellectual property (the “Intellectual Property”) and any reproductions of copyright works in the thesis, for example graphs and tables (“Reproductions”), which may be described in this thesis, may not be owned by the author and may be owned by third parties. Such Intellectual Property and Reproductions cannot and must not be made available for use without the prior written permission of the owner(s) of the relevant Intellectual Property and/or Reproductions.

iv. Further information on the conditions under which disclosure, publication and commercialisation of this thesis, the Copyright and any Intellectual Property and/or Reproductions described in it may take place is available in the University IP Policy (see <http://documents.manchester.ac.uk/DocuInfo.aspx?DocID=24420>), in any relevant Thesis restriction declarations deposited in the University Library, The University Library’s regulations (see <http://www.library.manchester.ac.uk/about/regulations/>) and in The University’s policy on Presentation of Theses

## **Publication from this work**

Jun Long, Marco A. Rodriguez Frias, Khursiah Zainal Mokhtar and Wuqiang Yang, An Integrated ECT and Electrostatic Sensor for Particulate Flow Measurement, *IEEE International Conference on Imaging Systems and Techniques*, 16-18 Oct. 2018, Krakow, Poland (accepted)

## **Acknowledgement**

In the name of Allah, the Most Gracious, the Most Merciful.

To my respected parents, Zainal Mokhtar and Sarimah. To my brother, sisters and sister in law, Adnin, Annisa, Munirah and Anisah.

To Professor Wuqiang Yang for insightful discussion about the research and his guidance during my study at the University of Manchester. To Professor Haigang Wang for giving me the opportunity to conduct the research at the Institute of Engineering Thermophysics, Chinese Academy of Sciences.

To Professor Mohd Fua'ad Rahmat, Dr. Teimour Tajdari and Dr. Yasmin Abdul Wahab from Universiti Teknologi Malaysia, and Dr. Ku Nurul Edhura from the University of Manchester for their scientific advice and knowledge.

To Majlis Amanah Rakyat (MARA) for sponsoring my study at the University of Manchester.

To my colleagues and friends, Fafa, Jun Long, Mimi, Wen Bin, Marco, Meng Wu, Hanqiao Che and Zhen Ren, thank you for the valuable discussion and suggestion.

Finally, I dedicate this dissertation to the loving memories of my late mother, Ramlah.

# CHAPTER 1

## INTRODUCTION

### 1.1 Background

In many industries, information on material flow such as flow regime (Banasiak et al., 2014; Abdulkareem et al., 2015), material velocity (Chao et al., 2015; Li et al., 2016; Yang et al., 2016; Saoud et al., 2017), mass flow rate (Li et al., 2015; Foster-Turner and Hunt, 2015) and component concentration (Zainal-Mokhtar and Mohamad-Saleh, 2013; Wang et al., 2014; Sardeshpande et al., 2015) are important parameters for process interpretation to enact the safety and efficiency of industrial processes. These information are also useful for developing new process equipment and enhancing process operation. For instance, in gas/solids flows, information on solids velocity inside a pneumatic conveyor is essential to minimise energy consumption and to control the transport of solid particles. Meanwhile, information on solids concentration in gas/solids flows can be utilised along with solids velocity measurement to obtain the mass flow rate of solids, which is considered as an important parameter of a pneumatic conveying system as it contributes to acquisition of internal flow situation, reduction of energy cost and flow control. In any transport system, it is always desirable to measure the material transport rate in real time and without disturbing the flow. System operators tend to use load cells at the receiving tank/silo to monitor the mass of material transported (Barbir and Mathews, 2016). These load cells are very costly if the size of silo is very large. Hence, non-invasive electrostatic sensor and Electrical Capacitance Tomography (ECT) sensor have been used to obtain solids velocity and solids concentration, respectively, regarding gas/solids flows in process equipment.

Electrostatic sensor is suitable for measuring some processes where charge is generated such as in gas/solids flows. Meanwhile, ECT can be utilised in concealed industrial processes involving nonconductive materials, such as gas/solids. In addition, their simple structures, high sensitivity, less expensive and intrinsically safe make them ideal to be used in industrial processes.

The solids mass flow rate can be measured in two ways: by the direct method (Wang et al., 2018; Tombs et al., 2018; Zhang et al., 2018a) and the inferential method also known as indirect method (Carter and Yan, 2005; Sun et al., 2008; Li et al., 2015). The direct approaches of solids' mass flow rate measurement is more straightforward than indirect methods whereby the sensing elements respond directly to the mass flow rate through a sensing field of an indirect flow meter. Direct mass flow measurement based upon Coriolis force offers exceptional accuracy in single phase flow of liquids or

gasses. However, conventional Coriolis flow meters can only deal with liquid, but not with solids flow (O'Banion, 2013).

## **1.2 Problem and Motivation**

Direct measurement systems seem very attractive considering their ability to directly measure a mass flow rate. However, this method cannot be used for measuring solids flow rate. Hence, it is necessary to use an indirect method to measure the solids' mass rate. Currently, a new trend in sensor development in gas/solids flow measurement is to apply dual modality sensors. Many researches have carried out research into measurement of a mass flow rate using one type of sensor. However, one type of sensor may give inaccurate measurements. For example, ECT has demonstrated its capability to obtain material distribution in a cross-sectional area of process equipment but it still gives inaccurate measurement of solids velocity despite numerous modification have been made to improve image reconstruction algorithms. Thus, it is necessary to use a dual modality sensor to measure each flow parameter efficiently. It is also vital to choose a reliable sensor for each measurement and at the same time being cost effective. For many years, ECT has shown its capability in visualising the material concentration and electrostatic sensor has proven its ability in measuring the solids velocity accurately. Both the sensors are not only cost effective due to their simple structures but also robust. Therefore, an investigation on developing integrated ECT and electrostatic sensors for mass flow measurement is necessary.

## **1.3 Research Objectives**

This research work aims to develop an integrated ECT and electrostatic sensor assembly for measuring the mass flow rate of gas/solids flows. The objectives of the research are as follows:

- 1) To develop the mass flow rate sensor based on an ECT sensor and an electrostatic sensor
- 2) To optimise the electrode length and distance between upstream and downstream electrodes of electrostatic sensor
- 3) To develop novel mass flow sensor based on an ECT sensor and a symmetrical electrostatic sensor



## **1.4 Thesis Outline**

This chapter introduces the background and research work. It briefs on the background, problems and motivation, objectives and the scope of the research.

Chapter 2 gives a brief overview of electrostatic sensor and ECT, as these topics are the main subjects of the research. The Linear Back Projection (LBP) algorithm used in this research is explained in this chapter. Then, a discussion on the principle of mass measurement, solids velocity and solids concentration measurements are included.

Chapter 3 explains the measurement system of the integrated ECT and electrostatic sensors for gas/solids flow measurement built for standpipe of a circulating fluidised bed (CFB) and a gravity flow rig. The mass flow meters for both standpipe and gravity flow rig are first presented and briefly discussed. This is followed by an explanation on ECT sensor models and electrostatic sensor systems used for both process equipments. This section also includes a discussion on CFB and its sub part, a standpipe and the experimental setup for measuring the mass flow. Next, the development of mass flow meter on a gravity flow rig are explained.

Chapter 4 presents the results from electrostatic sensor and ECT sensor of gas/solids flows for standpipe. The experimental results for mass flow measurement based on ECT sensor and two sets of electrostatic sensor for a gravity flow rig are also presented. This includes discussion on optimum distance between upstream and downstream electrodes and electrode length.

Chapter 5 gives a brief summary on the research work. This is followed by the conclusions of the investigation based on the obtained results. The final section of this chapter outlines the possible future works that can be carried out based on the foundation of this work.

## CHAPTER 2

### LITERATURE REVIEW

#### 2.1 Electrostatic Sensor

When dry solids flow in a conveyor, the solids become charged for several reasons. The electric charge carried by the materials is due to particles colliding to each other, particles impact to the pipe wall and the friction between particles and air flow. Researchers have been taking advantage of these phenomena to develop electrostatic sensors which can be used in many applications such as measuring velocity and mass flow rate, determining material concentration and identifying material deposited on pipe wall. Principally, two electrodes, attached to a point of interest, act as signal collectors. These electrodes are connected to signal conditioning circuits. The circuit is used to convert the electrostatic charge to voltage signal. Since the nature of the electrostatic signal is very small, the circuit is also used to amplify the signal. Then, this signal conditioning circuit is linked to a data acquisition system to convert the voltage signal to digital signal so that it can be displayed in a computer. The fundamental of electrostatic sensor system is illustrated in Figure 2.1.

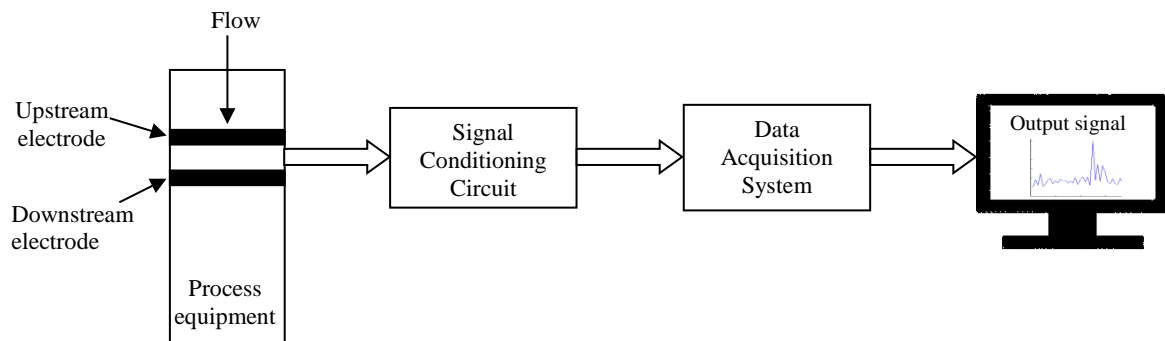


Figure 2.1: An electrostatic sensor system

Many industries utilised electrostatic sensor to provide measurement solutions that are efficient and cost-effective. Various researches have revealed plenty of electrostatic capabilities to determine or interpret a process in a pipe such as measuring solids/gas flow velocity in pipelines using cross-correlation technique (Coombes and Yan, 2016; Wang et al., 2017) or spatial filtering method (Wen et al. 2014), obtaining concentration profile-map utilising process tomography technique (Rahmat et al., 2009), measuring mass flow rate (Qian et al., 2017), estimating moisture content (Zhang et al., 2018b) and determining the particle mean size (Tajdari et al., 2014). Among the above applications, velocity measurement is one of an important process interpretation heavily researched in various industries dealing powder or biomass and coal (Wen et al. 2014; Coombes and Yan, 2016; Qian et al., 2014; Qian

et al., 2017; Wang et al., 2017). Velocity measurement can be obtained from combining electrostatic sensor technique with cross-correlation method as shown in Figure 2.2.

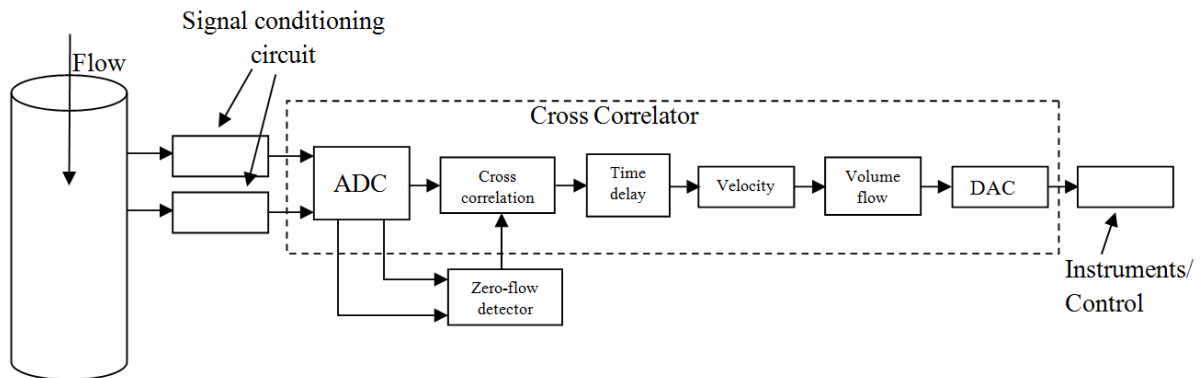


Figure 2.2: Subsystem of cross-correlation flow meter

Initially, the analogue electrostatic signals are converted by signal conditioning circuits into digital forms for their cross correlation function to be computed. After the cross correlation of the two signals is computed, the peak position of the resulting cross-correlation curve is detected to find the estimated flow transit time between the two electrodes. Next, the estimated transit time of the flow can be used to directly calculate the solids velocity if one knows the physical dimension of the installation and include any calibration factors.

Each time velocity is measured using an electrostatic sensor, there will be discrepancy between mean particle velocity and correlation velocity. This happens due to non-uniform spatial sensitivity of electrode used. Spatial sensitivity of electrostatic sensor needs to be made uniformed and can be achieved by optimising the size of electrode. One of the significant factors to achieve a more uniform spatial sensitivity distribution is the length of electrodes (Heydarianasl and Rahmat, 2017). When more uniform spatial sensitivity distribution is achieved, the discrepancy between mean particle velocity and correlation velocity can be minimised.

Another vital factor in designing the electrostatic sensor is the distance between upstream and downstream electrodes. It is vital to choose suitable distance between those electrodes as the distance will affect the cross-correlation velocity. Higher distance will lead to lower cross-correlation coefficient which also means the similarity of signals between those electrodes is also lower. If the two electrodes are placed closer to each other, the similarity of the signals will be higher and higher cross-correlation coefficient will be achieved. However, if the spacing between the electrodes is too closed, this will cause the electric field on both electrodes to interact (Heydarianasl and Rahmat, 2014).

## 2.2 Electrical Capacitance Tomography (ECT)

The origin of the word "tomography" is from Greek words; "tomos" meaning slice or section and "graphe" meaning drawing. The tomographic measurement technique was first applied to medical imaging in 1970's. A Computerised Tomography (CT) machine uses a radiation source (i.e. x-ray) that rotates around a human body to obtain a set of measurements. These measured data are used to reconstruct a cross-section of the human body.

In the 1980s, the tomographic technique was introduced for imaging industrial processes. Known as Process Tomography (PT), it has become increasingly popular with its adoption and implementation based on various modalities and techniques. However, the most conspicuous PT techniques are based on measurement of electrical properties through utilisation of permittivity, conductivity and permeability of materials under investigation, i.e. by measuring capacitance, conductance, or inductance. Of these electrical tomographic techniques, ECT is in the most advanced state of research and development for industrial applications. An ECT sensor normally consists of copper plate electrodes, which are sensitive to dielectric constants of materials. An ECT sensor is mounted equidistantly around the periphery of an insulating process at a point of interest. Because different materials have different dielectric constants known as relative permittivities, the distribution of a two component flow within an ECT sensing region produces a change in capacitance between two electrodes. The effective capacitance that occurs between pairs of electrodes is measured. Then, an appropriate image reconstruction algorithm is used to reconstruct an image of such material distribution using the capacitance measurements. The tomographic images obtained from the imaging process are not only useful in determining the flow regime but also the vector velocity and component concentration in process vessels and pipelines. ECT has been applied in various industrial processes, such as gas/solid distribution in pneumatic conveyors (Yang et al., 2014; Wang et al., 2015; Li et al., 2016), fluidised beds (Li et al., 2018; Che et al., 2018; Weber et al., 2018), flame combustion (Gut and Wolanski, 2010; Liu et al., 2015), gas/liquid flows (Archibong-Eso et al. 2018; Omar et al., 2018), water/oil/gas separation process (Bukhari and Yang, 2006; Zhao et al., 2007; Jaworski and Meng, 2009; Li et al., 2013) and water hammer (Yang et al., 1996) . For more than 20 years, tomographic techniques have promised great potential in multiphase flow measurement as it possess advantages including no radiation, low cost, high time resolution, and tolerance to high pressure and high temperature.

Figure 2.3 shows an ECT system consisting of a sensor, a data acquisition system (DAS) and a computer. Differential voltages between all possible electrode combinations are measured by DAS, which is used to convert the ECT measurements into digital signal and sending the signal to the computer. The computer has two main functions. First, it controls the operations performed by the DAS. Second, by means of an appropriate algorithm, it uses the measured capacitance data to produce useful

information represented either qualitatively in the form of a reconstructed image of flow process and/or quantitatively in the form of flow parameter estimations.

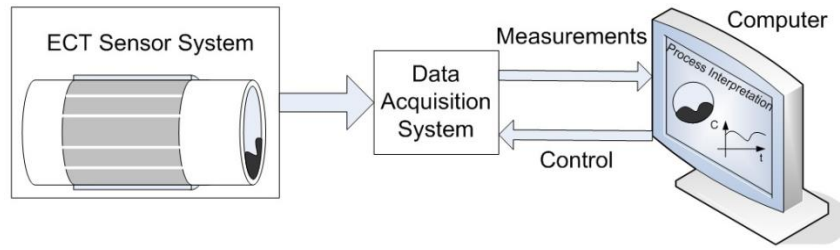


Figure 2.3: An ECT system

ECT is used to measure permittivity distribution of the contents inside a pipe by measuring the interelectrode capacitance. These inter-electrode capacitance values are very small, typically in the range of 0.01 pF to 1 pF (Marashdeh et al., 2008). There are various sensor design issues, which have to be considered, as they affect the performance of an ECT system.

### 2.2.1 Mathematical Formulation of the Sensor Model

The calculation of capacitance from a given permittivity distribution between two parallel plates capacitor can be obtained using

$$C = \frac{A\epsilon_0\epsilon_r}{d} \quad (2.1)$$

where  $A$  is the cross-sectional area of electrodes,  $\epsilon_0$  is the permittivity of free space and  $d$  is the distance between the electrodes. The dielectric constant  $\epsilon_r$  is the relative permittivity.

However, the multiple electrodes in an ECT sensor are in circle shape as shown in Figure 2.3. Also, ECT has its unique procedure to perform the capacitance measurements. Due to this complex shape of an ECT system, equation (2.1) cannot be used to calculate the capacitance from an ECT system.

Hence, an ECT sensor model is described using the electrostatic field theory and the solution can be calculated using Gauss's law for the electric field given by

$$\nabla \cdot D(x, y) = \rho_f(x, y) \quad (2.2)$$

where  $\rho_f(x, y)$  is the free charge density distribution.

In a 2D ECT sensor, the permittivity distribution is assumed to be isotropic and linear (Alme and Mylvaganam, 2006). Thus, the relationship between the electric displacement field distribution,  $D(x, y)$ , and electric field distribution,  $E(x, y)$ , can be described as

$$D(x, y) = \varepsilon_0 \varepsilon_r(x, y) E(x, y) \quad (2.3)$$

where the permittivity of free space  $\varepsilon_0$  is a constant and  $\varepsilon_r(x, y)$  is medium's relative permittivity distribution or dielectric constant distribution.

The electric field distribution is given by

$$E(x, y) = -\nabla\phi(x, y) \quad (2.4)$$

where  $\phi(x, y)$  is the electrical potential distribution.

Combining equations (2.2) until (2.4) yields

$$\nabla \cdot (\varepsilon_0 \varepsilon_r(x, y) \nabla\phi(x, y)) = -\rho_f(x, y) \quad (2.5)$$

Assuming there is no free charge inside an ECT sensor, the equation (2.5) becomes

$$\nabla \cdot (\varepsilon_0 \varepsilon_r(x, y) \nabla\phi(x, y)) = 0 \quad (2.6)$$

Equation (2.6) is the linear Poisson's equation and the equation also indicates that the conductivity of the medium inside the ECT sensor is negligible.

By applying Gauss's Law, the charge sensed by electrode  $j$  when electrode  $i$  is energised can be calculated using

$$Q_{ij} = \oint_{\Gamma_j} \varepsilon_0 \varepsilon_r(x, y) E(x, y) \cdot \hat{n} dl \quad (2.7)$$

where  $\Gamma_j$  is the surface of receiving electrode and  $\hat{n}$  is a unit vector normal to  $\Gamma_j$ .

The capacitance between electrode  $i$  and  $j$ ,  $C_{ij}$ , can then be calculated using

$$C_{ij} = Q_{ij}/V_{ij} \quad (2.8)$$

where  $V_{ij}$  is the voltage between the source electrode  $i$  and the detecting electrode  $j$ .

Using equations (2.4), (2.7) and (2.8), the measured capacitance for  $N$ -electrode capacitance (when electrode  $i$  is the source and electrode  $j$  is the detector) can be found by

$$C_{ij} = -\frac{\epsilon_0}{V_{ij}} \oint_{\Gamma_j} \epsilon(x, y) \nabla \phi(x, y) \cdot \hat{n} dl \quad (2.9)$$

A similar definition of the capacitance between a pair of electrodes was proposed by Xie et al. (1990) with more factors considered.

## 2.2.2 General Principles of ECT Measurement

Each time when a measurement is made, one of the electrodes acts as an excited electrode, on which a voltage is applied, and the remaining electrodes are the sensing electrodes held at the ground potential. For instance, for a 12-electrode ECT sensor, if electrode 1 is the excited electrode, all other 11 electrodes become the sensing electrodes. As such, DAS first measures the inter-electrode capacitance between electrodes 1 and 2 ( $C_{1,2}$ ), then between electrodes 1 and 3 ( $C_{1,3}$ ), and so forth up to 1 and 12 ( $C_{1,12}$ ). Then, the measurement procedure continues with the inter-electrode capacitance between electrodes 2 and 3 ( $C_{2,3}$ ), and so forth up to 2 and 12 ( $C_{2,12}$ ). The measurement process continues until the inter-electrode capacitance between all possible pairs of electrodes are measured. The excited electrodes and the capacitance measurements produced are shown in Table 2.1.

The total number of capacitance measurements  $M$  can be calculated using (Alme and Mylvaganam, 2006)

$$M = \frac{N(N-1)}{2} \quad (2.10)$$

where  $N$  is the number of electrode used in an ECT sensor. Therefore, for an 8-electrode sensor, there are 28 possible values of inter-electrodes capacitances.

Table 2.1: Capacitance measurements produced from pairs of excited and other electrodes

Excited Electrode	Pairs of Capacitance Measurements
1	$C_{1,2}$ $C_{1,3}$ $C_{1,4}$ $C_{1,5}$ $C_{1,6}$ $C_{1,7}$ $C_{1,8}$
2	$C_{2,3}$ $C_{2,4}$ $C_{2,5}$ $C_{2,6}$ $C_{2,7}$ $C_{2,8}$
3	$C_{3,4}$ $C_{3,5}$ $C_{3,6}$ $C_{3,7}$ $C_{3,8}$
4	$C_{4,5}$ $C_{4,6}$ $C_{4,7}$ $C_{4,8}$
5	$C_{5,6}$ $C_{5,7}$ $C_{5,8}$
6	$C_{6,7}$ $C_{6,8}$
7	$C_{7,8}$

### 2.2.3 ECT Sensor and Normalisation of Capacitance Measurement

As shown in Figure 2.4 (a), an ECT sensor uses 8 electrodes mounted equidistantly around the periphery of an insulating pipe. The primary electrodes are used to accumulate charges to generate an electric field to measure capacitance. The outer screen placed around the electrodes shields the sensor from the effects of extraneous variation in the stray capacitance to earth. Stray capacitance is an undesirable capacitance that usually occurs within the CMOS switches in the measuring circuit, within the cables connecting the electrodes to the measuring circuits and the sensor screen (Yang, 1995).

In Figure 2.4 (a),  $R_1$  is the inner radius within the sensing region,  $R_2$  is the outer radius, which extends from the middle point of a pipe to the ECT sensor system and  $R_3$  is the radius of electrode screen, which shields the whole sensor system. The fringe effect occurs when the electric fields at both ends of ECT electrodes spread outside the interior of the pipe. The fringe effect will cause non-uniform<sup>m</sup> sensitivities along the axial direction (Yan et al., 1999; Peng et al., 2005). In addition, the sensor will detect medium outside its sensing area and consequently will appear in reconstructed ECT images (Yan et al., 1999). Hence, two grounded end screens are placed at the ends of electrodes as shown in Figure 2.4 (b) to neutralise the electric fields lines, and eventually the capacitance measured between these electrodes is due only to the field lines that cross the region under study. In addition, the work by Olmos et al. (2006) showed that the quality of the image obtained with the shielded sensor was clearly better than that reconstructed with the non-shielded one.

A vital step in planning a successful ECT application is the proper design of an ECT sensor. Various design parameters of ECT sensors interact and affect the overall sensor performance and various design rules (Yan et al., 1999; Alme and Mylvaganam, 2006; Yang, 2010) have been developed, which allow a proper ECT sensor to be constructed for a specific application. For instance, the number and the size of measuring electrodes are two design parameters of an ECT sensor, which are application-dependant. With the increase in the number of electrodes, the number of independent measurements increases and



a higher resolution image can be expected. However, too many electrodes results in smaller electrode size, which leads to lower measurement sensitivity compared to a sensor with fewer electrodes. Sensitivity can be increased by using larger electrodes though this will decrease spatial resolution and therefore, a good image cannot be obtained.

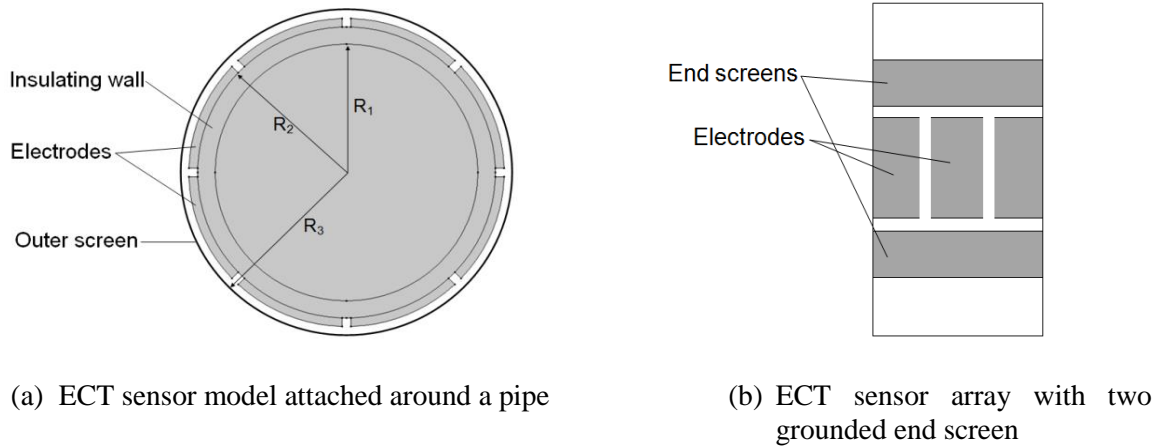


Figure 2.4: ECT sensor

The measured ECT data are usually normalised before being used in any application. Initially, the process is carried out by obtaining the capacitance measurement when an ECT sensor is full with a higher permittivity material and followed by full of a lower permittivity material. Then, the capacitance measurement of various flow patterns under investigation is attained. Based on the assumption that the distribution of the two materials is in parallel (see Figure 2.5) and hence, the normalised capacitance is a linear function of the measured capacitance (Yang and Byars, 1999).

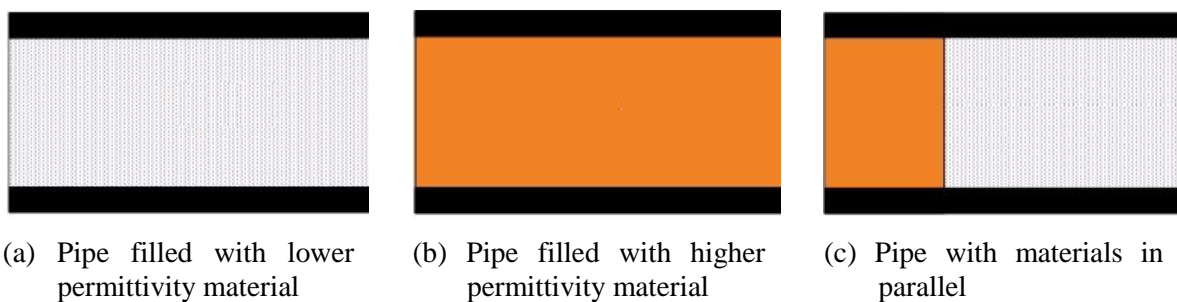


Figure 2.5: Schematic diagram of ECT sensor cross-section

The normalisation equation (Xie et al., 1989) is given by

$$\lambda_{ij} = \frac{c_{ij}^m - c_{ij}^l}{c_{ij}^h - c_{ij}^l} \quad (2.11)$$

where  $\lambda_{ij}$  is the normalised capacitance between a pair of electrodes  $i$  and  $j$ ,  $C_{ij}^m$  is the measured capacitance,  $C_{ij}^l$  is the capacitance when pipe is filled with lower permittivity material and  $C_{ij}^h$  is the capacitance when pipe is filled with higher permittivity material.

#### 2.2.4 Sensitivity Matrix

To obtain permittivity distribution from capacitance measurements is a complicated process and its solution requires knowledge of inverse problems. One of the methods to solve inverse problems is by utilising a sensitivity matrix. In ECT, a sensitivity matrix needs to be calculated before reconstruction of ECT images. Image reconstruction in ECT usually employs sensitivity matrices that map the relation between the permittivity distribution and the measured capacitance. The change in capacitance measurements are not only caused by an object with a given permittivity, the variation in measured capacitances are also depends on the location of the object in the sensing area. Sensitivity of an ECT sensor is largest near the electrodes and diminishes towards the centre. All these information are stored in sensitivity map files. Typically, a sensitivity matrix is obtained by subdividing the imaging area into small pixels and determining the capacitance changes of an electrode pair in each pixel due to a small perturbation of each pixel with respect to the empty background (i.e. the imaging area is filled with low permittivity material). Based on the potential distribution inside the sensing area, the sensitivity map can be easily calculated by numerical simulation.

$$S_{ij}(x, y) = \iint_{p(x,y)} \frac{E_i(x,y)}{V_i} \cdot \frac{E_j(x,y)}{V_j} dx dy \quad (2.12)$$

Where  $S_{ij}(x, y)$  is the sensitivity between the  $i$ th electrode and the  $j$ th electrode at pixel  $p(x, y)$ , and  $E_i(x, y)$  and  $E_j(x, y)$  are the electric field strength when the electrodes are applied voltages  $V_i$  and  $V_j$  respectively for excitation in turn.

#### 2.2.5 Image Reconstruction Algorithms

In ECT, the sensing electronics measure variations in capacitance between pairs of electrodes, which are placed around the periphery of a pipe or vessel under investigation. These measurements are then used to reconstruct the cross-sectional permittivity distribution as a presentation of the material distribution inside the sensing area via a specific image reconstruction algorithm. However, two major difficulties are associated with the reconstruction process. First, the number of measured independent capacitance measurement is far less than the number of unknown image pixels, and therefore the

problem is severely under-determined. Thus, there is no analytical solution for the inverse problem. Secondly, due to the ill-posed and ill-conditioned properties of the reconstruction process, the reconstructed results are sensitive to raw capacitance measurement noise. To address these problems, different reconstruction techniques has been reviewed extensively by Isaksen (1996), and Yang and Peng (2003). Isaksen (1996) reviewed LBP, Model-based reconstruction (MOR), algebraic reconstruction technique (ART), use of look-up table and artificial neural network. Yang and Peng (2003) covered the LBP, SVD, Tikhonov, iterative Tikhonov, Landweber and projected Landweber. Both papers have highlighted the pros and cons of each algorithm they discussed. Each image reconstruction algorithms can be widely categorised into non-iterative and iterative techniques.

- **Linear Back Projection (LBP)**

The Linear Back Projection (LBP) algorithm (Xie et al., 1989) was the first and simplest reconstruction algorithm for ECT. It uses binary sensitivity information whereby the sensitivity is equal to '1' if a particular material exists in a pipe. Otherwise, the sensitivity is set to '0'. A direct consequence of this technique is that images produced appear to be seriously distorted (Xie et al., 1992). The work by Huang et al. (1988) and Xie et al. (1989) were the earliest application of LBP to solve the inverse problem in ECT. Xie et al. (1992) overcome the issue of distorted images employing the full sensitivity information instead of its binary representations. Despite its low accuracy reconstructed images, the algorithm is still widely used due to its simplicity and thus short computational time. Using a sensitivity map and normalised capacitance measurements, the approximation of the permittivity distribution can be calculated using the shaded colour level of the pixel, which can be expressed as

$$\hat{g}(p) = \frac{\sum_{i=1}^{N-1} \sum_{j=i+1}^N \lambda_{ij} S_{ij}(p)}{\sum_{i=1}^{N-1} \sum_{j=i+1}^N S_{ij}(p)} \quad (2.13)$$

where  $p$  is a pixel element,  $N$  is the number of electrodes used,  $\lambda_{ij}$  is the normalised capacitance measurement between electrodes  $i$  and  $j$ , and  $S_{ij}(p)$  is the sensitivity value between electrodes  $i$  and  $j$  for pixel element  $p$ .

Figure 2.6 illustrates a flowchart for the LBP algorithm. Firstly, the raw capacitance measurement corresponding to each electrode pair  $i$  and  $j$  are normalised. Then, equation (2.13) is solved using the normalised capacitance measurement and sensitivity matrix calculated using equation (2.12). Finally, the calculated shaded colour level is displayed on a computer. Since the vectors used in the calculation are normalised values, the shaded colour level image should fall between '0' and '1' if the system is linear. However, the equation (2.13) can give the results of grey level values of  $\hat{g}$  smaller than '0' or

larger than '1'. The reason that the normalised capacitance  $\lambda_{ij}$  used in equation (2.13) may have overshooting (value larger than 1) and undershooting (value smaller than 0) causes by the nonlinear relationship between capacitance and permittivity distribution. Over- and under-shootings may cause poor quality images because shootings introduced unwanted values in grey level values of  $\hat{g}$  (Xie et al. 1992).

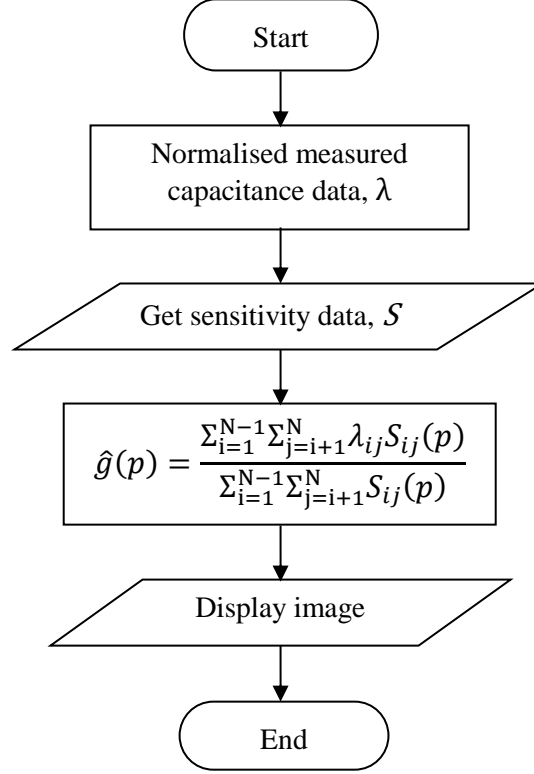


Figure 2.6: Flowchart of LBP image reconstruction algorithm

The overshooting can be eliminated by using the truncation operation (Isaksen and Nordtvedt, 1993)

$$\lambda_{ij} = 1, \text{ if } \lambda_{ij} > 1 \quad (2.14)$$

The work by Xie et. al. (1992) had shown that a threshold operation could further improve the reconstructed image by eliminating spurious low shaded colour level objects in the image. Threshold operation maps each  $\hat{g}$  to values based on a convex set based on (Xie et al., 1992),

$$\hat{g}_{new}(p) = \begin{cases} \hat{g}_{new}(p) = 0, & \text{if } \hat{g}(p) < \eta \\ \hat{g}_{new}(p) = \hat{g}(p), & \text{otherwise} \end{cases} \quad (2.15)$$

where  $\eta$  the threshold level is given by

$$\eta = (1 - 0.5\alpha)\zeta, (0 \leq \eta \leq 1) \quad (2.16)$$

and  $\alpha$  and  $\zeta$  are given by

$$\alpha = AVG[|\lambda_{ij}|; \{\lambda_{ij} = 1, \text{if } \lambda_{ij} > 1\}] \quad (2.17)$$

$$\zeta = AVG[\hat{g}(p); \{\hat{g}(p) > 0\}] \quad (2.18)$$

where AVG is the average operator.

### 2.3 Principle of Mass Flow Measurement

Mass flow measurement is very important in many applications such as mixing, blending and ratio control in the petrochemical, agricultural, aggregate, food and pharmaceutical industries. For instance, the aim of mixing process in the food industry is to combine multiple ingredients with an initial heterogeneous mixture to produce an optimum homogeneous mixture and finally achieved food product specification. Thus, the knowledge of the mass flow can aid in controlling the ratio of ingredients (e.g. fats, protein, solids, etc.) involved. Too much or too little ingredients being added to the mixture will result in poor quality food product. Meanwhile in the petrochemical industry, blending or mixing is carried out to obtain an efficient combustion. Hence, from the mass of each element, the accurate amount of elements, such as sub bituminous and bituminous, coal can be determined.

The mass of solid particles over the cross-section of a pipe can be deduced from the particle velocity and concentration,

$$m = \rho \cdot A \cdot v \cdot t \cdot \beta \quad (2.19)$$

where  $m$  is the mass of the solid particles,  $\rho$  is the particle density,  $A$  is the cross-sectional area of a process equipment,  $v$  is the particle velocity,  $t$  time taken for ECT sensor to acquire ECT data for each measurement and  $\beta$  is the solid concentration. The mass of particular solid can be calculated using equation (2.19) when solids velocity and solids concentration are measured using particular flow meter. In this work, solids velocity is measured using electrostatic sensor whereas solids concentration is determined with an aid of ECT sensor.

### 2.3.1 Velocity Measurement and Cross-correlation Technique

In the powder industry, velocity of particles in a gas/solids flow is one of the important parameters. The variation in velocity has a dramatic effect on the sensor output signal components both in the time and the frequency domains. There are two main techniques that can be used along with electrostatic sensors for particle velocity measurement: the cross-correlation technique and the spatial filtering method. The cross-correlation technique employed two identical electrodes placed and aligned in one line along the flow direction over a distance from each other as shown in Figure 2.7.

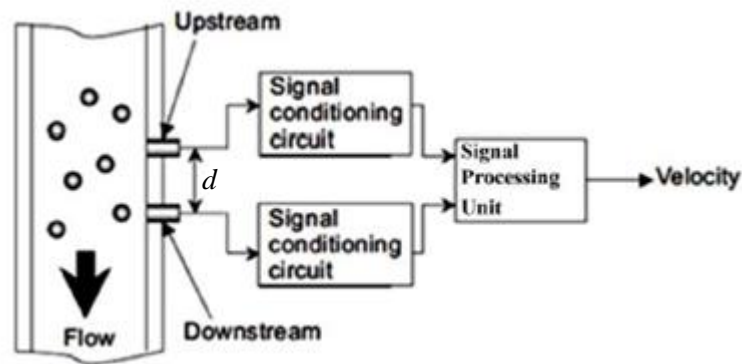


Figure 2.7: Velocity measurement using the cross-correlation technique

To cross-correlate the sensor outputs, the time delay  $\tau$  needs to be taken by the particle to cover the distance between the upstream and downstream electrodes (Yan and Ma, 2000; Coulthard et al., 2012). The velocity can then be calculated from the known  $\tau$  and the distance between electrodes. This technique was first used by Beck and Plaskowski (1987). Next, it had been employed by Gajewski et al. (1990) and Gajewski et al. (1993). Later Gajewski (1994) used it for the particle velocity measurement, which utilised ring electrodes. Ma and Yan (2000) designed a commercial prototype of a velocity measurement system using the cross-correlation technique. The prototype was tested on the pneumatic particle conveyor, showing a response time of less than 2.5 s and repeatability better than  $\pm 2\%$ . The cross-correlation technique also has been used by Yan et al. (2010), Rodrigues and Yong (2012) and Hu *et al.* (2016) and for strip and cable speed measurement in the electrical and fibre-optic cable industries. Xiangchen and Yong (2012), Qian *et al.* (2012) and Wang *et al.* (2014) used an array of electrostatic sensors instead of applying two electrodes, to attain a better accuracy. In this method, cross-correlation of the output signals from every two adjacent electrodes is calculated, and then the measurement results are obtained from a data fusion algorithm.

The spatial filtering method relates the frequency components of the output signal of an electrostatic sensor to the particle velocity. Hammer and Green (1983) showed that the particle velocity passing through a capacitive sensor, which has the similarity in term of function to the electrostatic sensor, has

direct relation with the frequency component of the output signal. Yan et al. (1995) and Gajewski (1996) also showed the same relation occurs for electrostatic sensors. Zhang (2002) proposed mathematical model indicating that a single particle velocity that crossed an electrostatic sensor has a direct relation with the frequency at peak of the signal power spectrum density (PSD). In higher velocities, the particle induces the electrostatic noise to the electrode with the higher frequency. Moreover, the advantage of this method is its simplicity due to using a single electrode. However, in the case of particle dense flow velocity in pneumatic conveyor measurement, this method has a broad spectral bandwidth that reduces the frequency reading accuracy. This may result in measurement errors. Xu et al. (2012) and Li et al. (2012) proposed a new method based on the spatial filtering technique using two sensor arrays whereas Li et al. (2014) used eight sensor arrays with five electrodes in each sensor array to investigate the spatial filtering characteristics of the electrostatic sensor array. Their results showed that sensor arrays together with a differential amplifier gave a narrow spectral bandwidth, indicating that the frequency at the peak of the power spectral density is directly related to particle flow velocity (Yang et al., 2016).

The correlation velocity measurement technique is based on similarity analysis of two signals derived from the upstream and downstream electrodes and on the calculation of the transit time. The cross-correlation function  $R_{xy}$  between the electrostatic signals derived from upstream electrode and downstream electrode can be obtained as

$$R_{xy}(\tau) = \lim_{T \rightarrow \infty} \frac{1}{T} \int_0^T x(t)y(t + \tau)dt \quad (2.20)$$

where  $x(t)$  and  $y(t)$  are the signals from upstream and downstream electrodes, respectively.  $T$  represents the integral time.

When the same particles pass through upstream and downstream electrodes,  $x(t)$  is similar to  $y(t)$  and just lagging behind a certain time  $\tau_0$ . The time delay  $\tau_{xy}$  corresponding to the peak position of the cross-correlation function  $R_{xy}$  is an estimated value of the transit time  $\tau_0$ . The cross-correlation velocity  $v_{xy}$  can be calculated as

$$v_{xy} = \frac{d}{\tau_{xy}} \quad (2.21)$$

where  $d$  represents the distance between upstream and downstream electrodes.

### 2.3.2 Particle Concentration Measurement

Solid concentration is one of the most important parameters in gas/solid flows in process equipment. The objective is usually to maximise it. Concentration has a major influence on the numerical values of some of the other constituent terms required for equipment modelling. For instance, non-uniform material distribution of roping flow (see Figure 2.8) through a bend often leads to poor gas and solids ratio, accelerates erosion product degradation (Dhodapkar et al., 2009; Ghafari and Sharifi, 2017). Other than that, the solids velocity can be so significantly reduced once the materials exit the bend (Klinzing et al., 2010; Tripathi et al., 2018). This reduced suspension velocity can cause a large bed deposit occurring immediately downstream of the bend (Klinzing et al., 2010). Solids deposition in a pipeline can affect the operation of solids flow in a pneumatic conveying system, resulting in ineffective transport of materials along the pipe or severe pipe blockage. Apart from that, the non-uniform flow pattern present real difficulties to achieve accurate measurement as the flow profile varies with the pipe runs and loading. Although the solids concentration is constant, the changes in solids distribution (i.e. flow regime) will change the gas/solids flow meter's reading. Hence, solids concentration is an important concept to understand and quantify.

Although there are various techniques can be employed to measure the solid concentration, ECT measuring technique is a highly attractive technique due to its capability at obtaining measurements non-invasively, non-intrusively and with no radiation involved, unlike other conventional methods. Image reconstruction method is usually adopted to measure solid concentration. A cross-sectional image can be reconstructed using ECT data with an aid of an image reconstruction algorithm. Jaworski and Dyakowski (2001) reconstruct images of gas/solids dense flow in pneumatic conveying system using ECT sensor. ECT images of various flow structures in vertical and horizontal pipe are similar with images produced by high-speed photographic technique. Unlike photographic method, ECT also gives valuable insight of the internal structures of flow instabilities such as plug and slug flows. Wang et al. (1995) was the first to use ECT for fluidise bed reactor by analysing solid particle concentration and its variation in different fluidisation regimes namely bubbling, slugging and turbulent. Subsequently, the research using ECT for solid concentration in fluidise bed reactors are conducted by many researchers (Makkawi and Ocone, 2007; Rautenbach et al., 2013; Yang et al., 2014; Chandrasekera et al., 2015; Li et al., 2016).



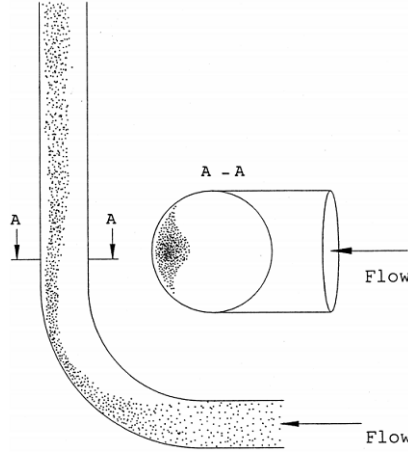


Figure 2.8: Schematic diagram of rope formed by flow through a bend

In principle, the concentration of contents of the ECT sensor can be calculated from normalised pixel values (i.e. grey level  $\hat{g}$ ). During an image reconstruction process, the imaging area is divided into a number of square pixels and grey level of each pixel represents the value of concentration for that pixel. By averaging the total value of grey level for a required image frame, the mean concentration can be calculated. The mean concentration is given by

$$\beta = \frac{1}{k} \sum_{p=1}^k \hat{g}_p \quad (2.22)$$

where  $\beta$  is the mean concentration,  $\hat{g}_p$  is the grey level at the  $p$ th pixel and  $k$  is the total number of pixels. Generally, ECT sensor captured a very high number of frames in one second and thus, the mean concentration for one frame is

$$\beta_{one\ frame} = \frac{\text{Total concentration for all frames}}{\text{Number of frames}} \quad (2.23)$$

## CHAPTER 3

### EXPERIMENTAL SETUP AND INSTRUMENTATION

#### 3.1 Designed of Mass Flow Meter by ECT and Electrostatic Sensor

This sub-section aims to discuss the proposed mass flow measurement system consisting of ECT and electrostatic sensors. There are two mass flow meter designs that are used on two different process equipments; namely a standpipe of a circulating fluidised bed (CFB) and a gravity flow rig. Figure 3.1 illustrates the proposed mass flow measurement system for the standpipe comprises of a 12-electrode ECT sensor and an electrostatic sensor to measure the solids concentration and solids velocity, respectively.

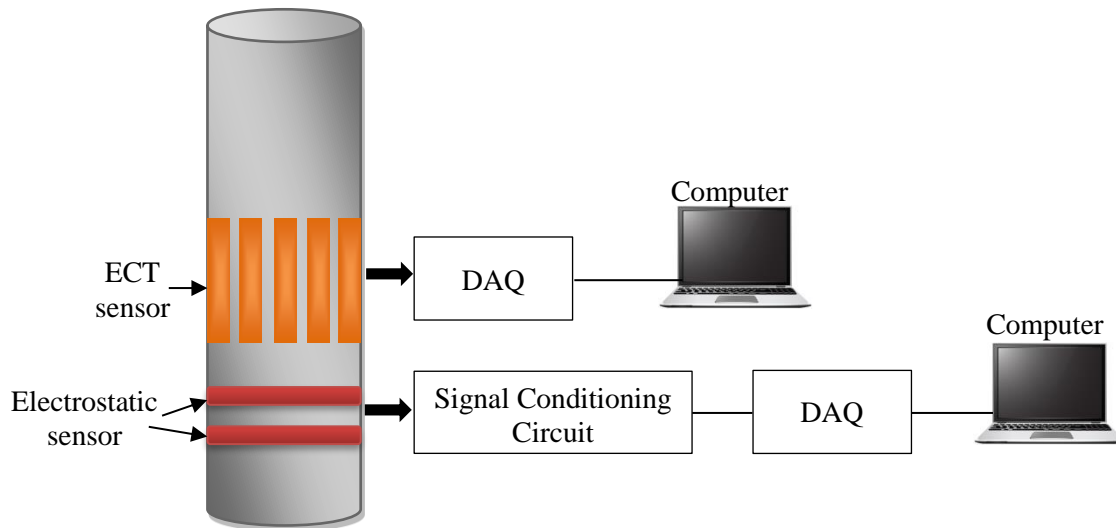


Figure 3.1: Mass flow measurement system for standpipe

It is extremely difficult to keep a constant flow rate of gas/solids flow for an experimental setup shows in Figure 3.1. This is due to the inconstant of solids velocity along the pipe. Hence, two sets of electrostatic sensor are placed with equal distance from the ECT sensor at each end of the ECT sensor. The reason for using two sets electrostatic sensors at each end of ECT sensor is to deal with solids velocity before and after the ECT sensor. Figure 3.2 shows the mass flow measurement system for gravity flow rig consisting of an 8-electrode ECT sensor and two sets of electrostatic sensor. To build such sensor arrangement, the investigation work stages require optimising the electrode length of electrostatic sensor and optimising the distance between upstream and downstream electrodes of electrostatic sensor.

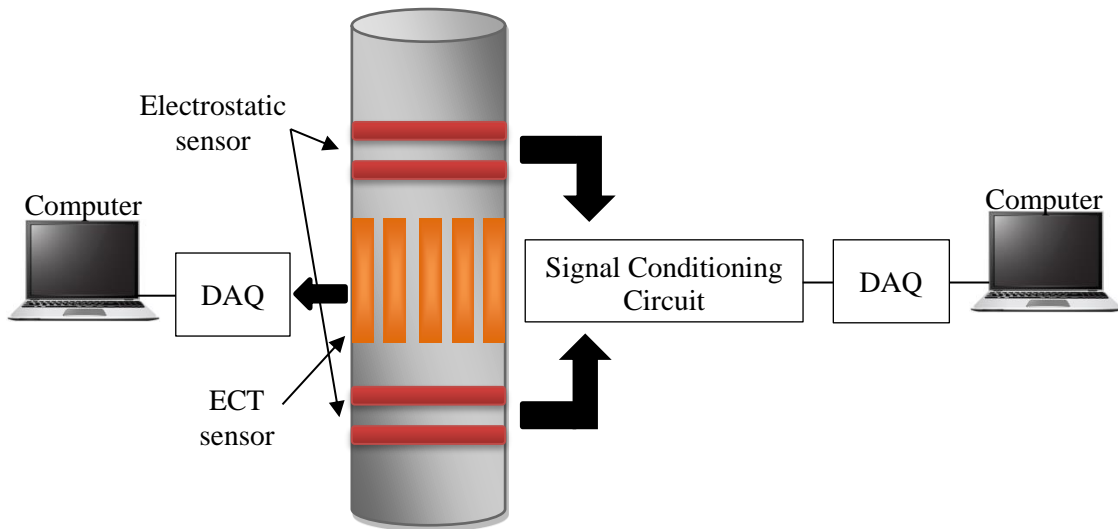


Figure 3.2: Mass flow measurement system for gravity flow rig

### 3.2 ECT Sensor Model

As stated in sub-section 3.1, a 12-electrode and an 8-electrode ECT sensors are built for measuring the solids concentration on standpipe and gravity flow rig, respectively. Both ECT sensor models are shown in Figure 3.3. The electrodes of both ECT sensors are made of copper and they are mounted on the outer surface of the standpipe and gravity flow rig. All the electrodes for both ECT sensors are covered in a metal shield to isolate them from any external electromagnetic interference.

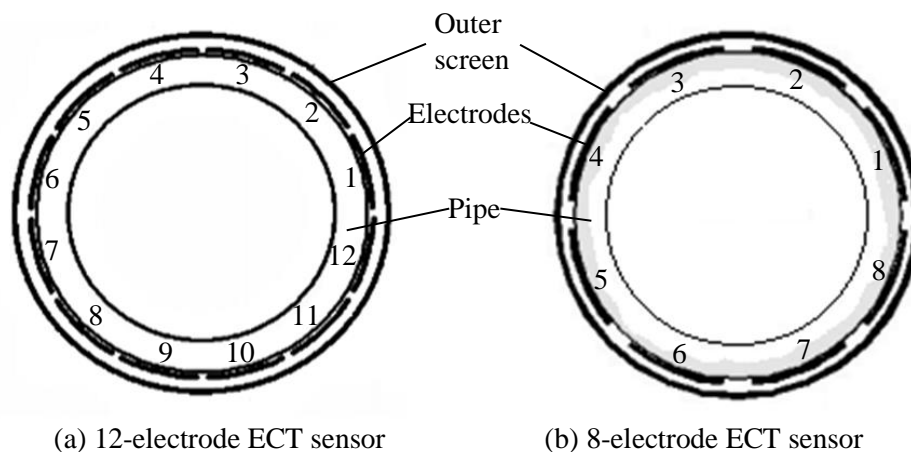


Figure 3.3: ECT sensor model used for mass flow measurement on standpipe and gravity flow rig

The number of electrodes of ECT sensor for standpipe is chosen to be 12 electrodes. The choice in the number of electrodes is a trade-off between resolution, sensitivity and image capture rate. More sensing electrodes produces better resolution images. However, the measurement sensitivity is lower because

the size of electrodes becomes smaller and at the same time reduces the capturing rate. The sensitivity of the sensor and the image capture rate can be increased by using bigger electrode size, though this will decrease the image resolution (Mohamad et al., 2011). Normally, 8 electrodes is not enough to provide sufficient data (i.e. low resolution) for an accurate interpretation or image reconstruction. On the other hand, 16-electrodes ECT decreases the sensitivity of the sensor towards the materials being investigated. Therefore, the number of electrodes used for mass flow measurement in standpipe is 12 for a trade-off between sensitivity and resolution.

In most applications, the sensor diameter is between 50 mm and 1000 mm. More measurements can be made from a sensor of more electrodes. Therefore, there are usually 12 or 16 electrodes in the ECT sensor in order to achieve better axial resolution of reconstructed images. For gravity flow rig in this work, however, the tube with an inner diameter of 32 mm is small to employ a complex sensor configuration. Therefore, the ECT sensor in this work is composed of 8 electrodes (Cui et al., 2014).

To analyse the ECT system, it is preferable to have a mathematical model of the ECT sensor. This sensor model is used to simulate a real sensor. This means that it can to generate capacitance sensitivity distribution maps as well as to solve the ECT forward problem by calculating capacitances between all possible electrode pairs. It is difficult to calculate an inter-electrode capacitance, which relates with the relative permittivity distribution  $\epsilon_r(x, y)$  and potential distribution  $\phi(x, y)$ , by the Laplace equation for the geometry and the boundary conditions. Hence, a finite element method (FEM) software simulation package COMSOL Multiphysics is utilised to find the electrical field distribution.

The creation of a capacitance sensor model in COMSOL Multiphysics aims to attaining a method, from which numerical calculation can be carried out for the electric potential ( $\phi$ ) in the space of the sensor (Yang, 2010). The design process for an ECT sensor model consists of the following steps:

- geometry generation according to the dimensions to be simulated
- boundary conditions assignment
- assignment of physical conditions in sensor sub-domains or zones.

The detail of physical sensor can be found in Table 3.1.

Table 3.1: Physical ECT sensor parameters

Item	Parameter	
	ECT sensor on standpipe	ECT sensor on gravity flow rig
Number of electrode	12	8
Electrode length	5.0 cm	5.0 cm
Inner pipe diameter	6.0 cm	3.2 cm
Outer pipe diameter	6.5 cm	3.4 cm
Screen diameter	6.9 cm	4.4 cm

### 3.2.1 Sensitivity Matrix Generation

The following procedures are necessary to carry out the numerical simulation of the sensor using COMSOL Multiphysics:

- (a) Choosing the mode in electrostatic module.
- (b) Drawing the sensor geometries.
- (c) Generating the mesh.
- (d) Set electrical properties in the domain.
- (e) Set the boundary conditions.
- (f) Solve and find the field distributions.
- (g) Use the post-processing capabilities in COMSOL Multiphysics to compute capacitances and voltages.

In this work, besides screen, measurement electrodes and pipe, the geometry includes the spatial discretisation of the inner part of the sensor,  $64 \times 64$  square matrix has a number of 4096 pixels but only 3096 pixels contribute to represent the image plane and another 1000 pixels lie outside the pipe boundary. Figure 3.4 (b) shows the finite element meshing in 2D of 12-electrode ECT sensor as appear in COMSOL Multiphysics. Only finite element meshing of 12-electrode ECT sensor is presented because similar procedure is used for finite element meshing of 8-electrode ECT sensor.

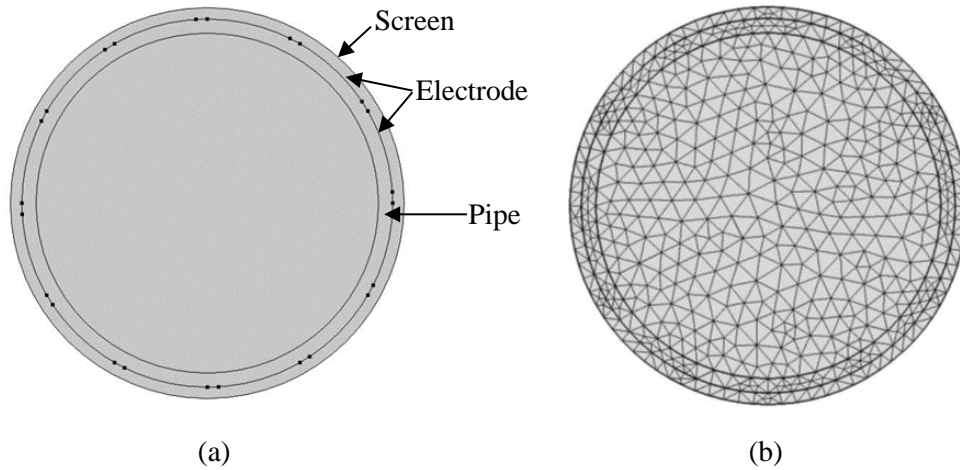
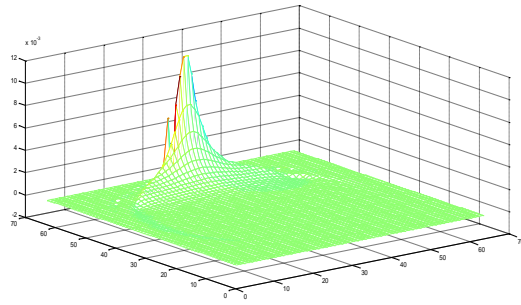
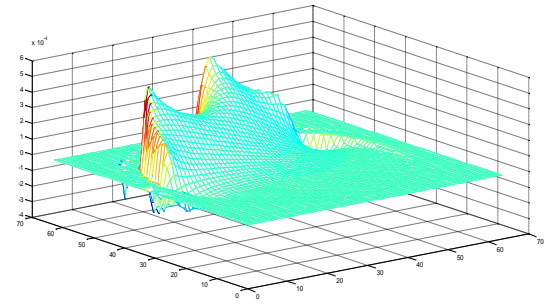


Figure 3.4: (a) 2D schematic diagram of 12-electrode ECT sensor drawn using COMSOL, and (b) FE meshing

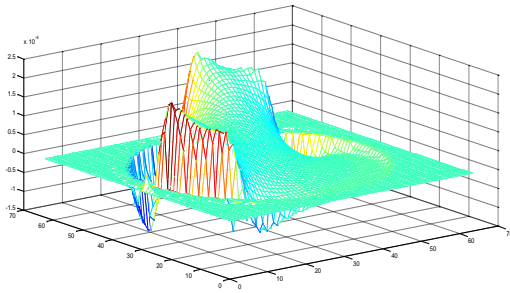
The simulation from COMSOL produces electrical potential distribution of all possible pairs of electrodes in each pixel. This electrical potential distribution is then used to generate sensitivity map based on equation (2.12) in sub-section 2.23. Although  $M$  sensitivity data are needed to present all electrode pairs, only  $N/2$  basic sensitivity maps are crucial. The other sensitivity maps can be obtained by rotating and mirroring these basic sensitivity maps (Huang *et al.*, 1988; Fasching *et al.*, 1991). Thus, four and six basic sensitivity maps are required for 8-electrode and 12-electrode ECT sensor, respectively. Figures 3.5 and 3.6 show the sensitivity maps for various electrode pairs for 8-electrode and 12-electrode ECT sensors, respectively. For all combination of electrode pairs, the area with the highest sensitivity is near the sensing electrode pairs. As the area moves toward the centre, the sensitivity becomes weaker. Due to this phenomenon, any permittivity distribution near the centre of the sensing region will be difficult to reconstruct compared to permittivity distribution near pipe wall. Also, negative elements may exist due to negative sensitivity values and if a small dielectric object is placed in a negative region, the capacitance will decrease instead of increase. This is a distinct feature of soft-field sensing.



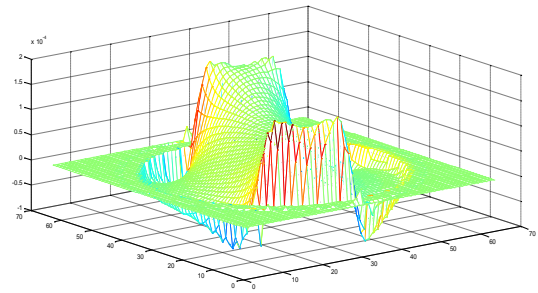
(a) Adjacent electrode pair



(b) A pair separated by one electrode

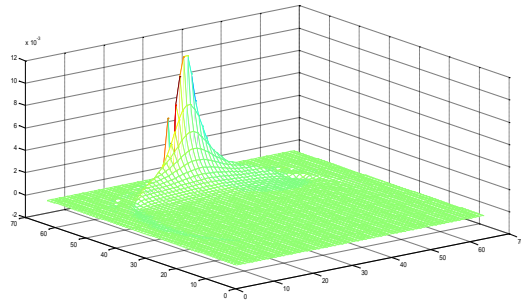


(c) A pair separated by two electrodes

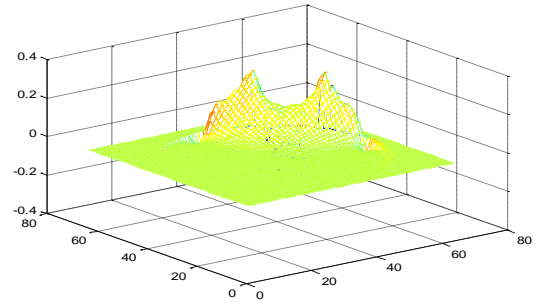


(d) A pair separated by three electrodes

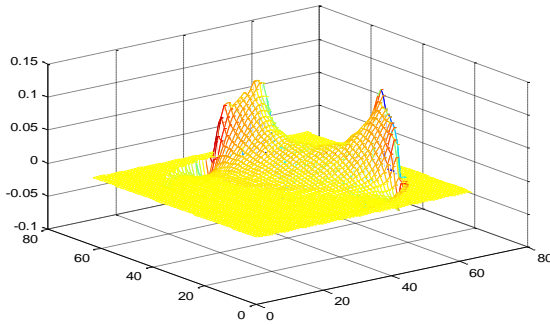
Figure 3.5: Sensitivity maps for 8-electrode ECT sensor



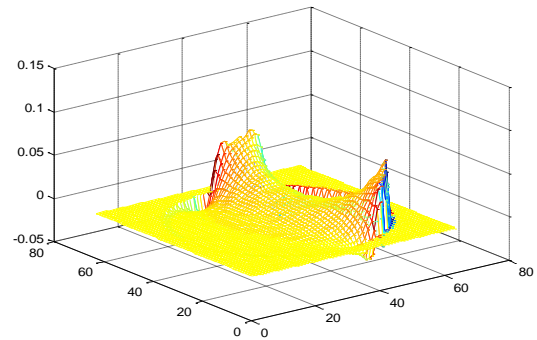
(a) Adjacent electrode pair



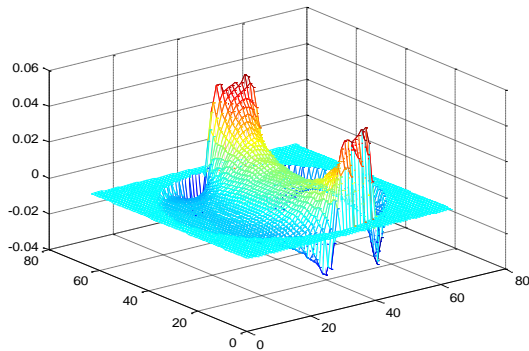
(b) A pair separated by one electrode



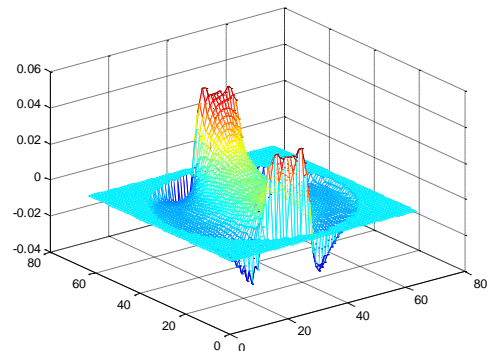
(c) A pair separated by two electrodes



(d) A pair separated by three electrodes



(e) A pair separated by four electrodes



(f) A pair separated by five electrodes

Figure 3.6: Sensitivity maps for 12-electrode ECT sensor

### 3.2.2 ECT Image Reconstruction

The LBP algorithm, which is the simplest ECT image reconstruction algorithm compared to other algorithms. The mathematical model of this non-iterative algorithm has been discussed in Chapter 2. There is no constant value that need to be set before starting its calculation. Using the normalised sensitivity values and the normalised capacitance between electrode pairs, the approximate shaded colour level of the permittivity distribution are obtained.



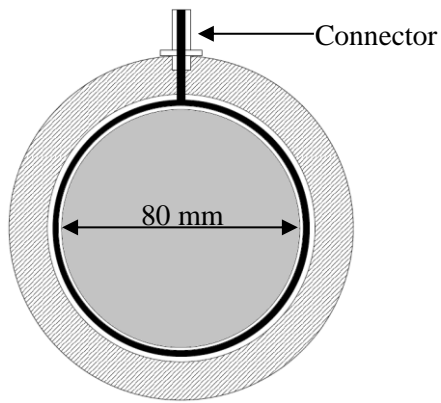
### **3.3 Electrostatic Sensor System**




This sub-section aims to discuss about the electrostatic sensor system used for measuring the solids velocity at CFB standpipe and gravity flow rig. As shown in Figures 3.1 and 3.2, this sensor can be divided into a sensing head, a signal conditioning circuit, a data acquisition system and a computer.

#### **3.3.1 Electrostatic Sensing Head**

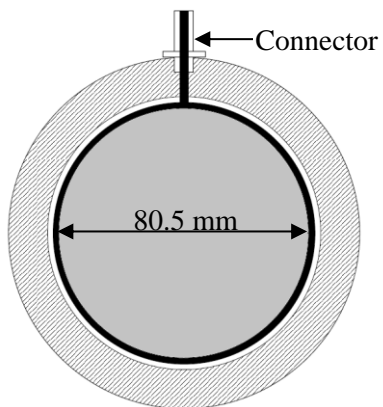
Two different electrostatic sensing heads utilised for velocity measurement on standpipe and gravity flow rig. Figure 3.7 shows cross-sectional views of an electrostatic sensing head used on standpipe with both (a) insulated and (b) exposed ring-shaped electrodes. Non-insulated electrodes are used in this study to measure the velocity of material. As can be seen, the difference between the exposed and insulated electrodes is the latter one has polyvinyl chloride (PVC) between the inner surface of the electrode and the particle flow. Each type of electrode consists of four electrodes with a distance between the sensor is 2 cm each. These electrodes are made of copper plate and are housed in a stainless steel sensing head, and insulated from each other using PVC.




Figures 3.8 and 3.9 show the longitudinal view of the sensing head. As shown in Figure 3.9, each electrode has an axial width of 2 mm to determine the velocity of particles by the cross-correlation technique. Also, each channel of electrode is separately transmitted to identical signal conditioning circuit. The electronic circuit essentially converts the weak electrostatic current signal into voltage signal. Then, the raw signal is converted to digital signal by a data acquisition system (DAQ) to be processed. Finally, the flow parameter is displayed by the computer.



Object	Description	Thickness (mm)	
		Between particle flow and electrode	Between electrode and sensing head
	Insulator PVC	0.5	1
	Ring-shaped electrode (brass)	1	
	Sensing head (metal)	2.5	
Connector	SMB jack straight connector		

(a)



Object	Description	Thickness (mm)	
		Between particle flow and electrode	Between electrode and sensing head
	Insulator PVC	1	
	Ring-shaped electrode (brass)	1	
	Sensing head (metal)	2.5	
Connector	SMB jack straight connector		

(b)

Figure 3.7: Cross-sectional views with descriptions of (a) insulated and (b) exposed ring-shaped electrodes



Figure 3.8: Photo of the sensing head

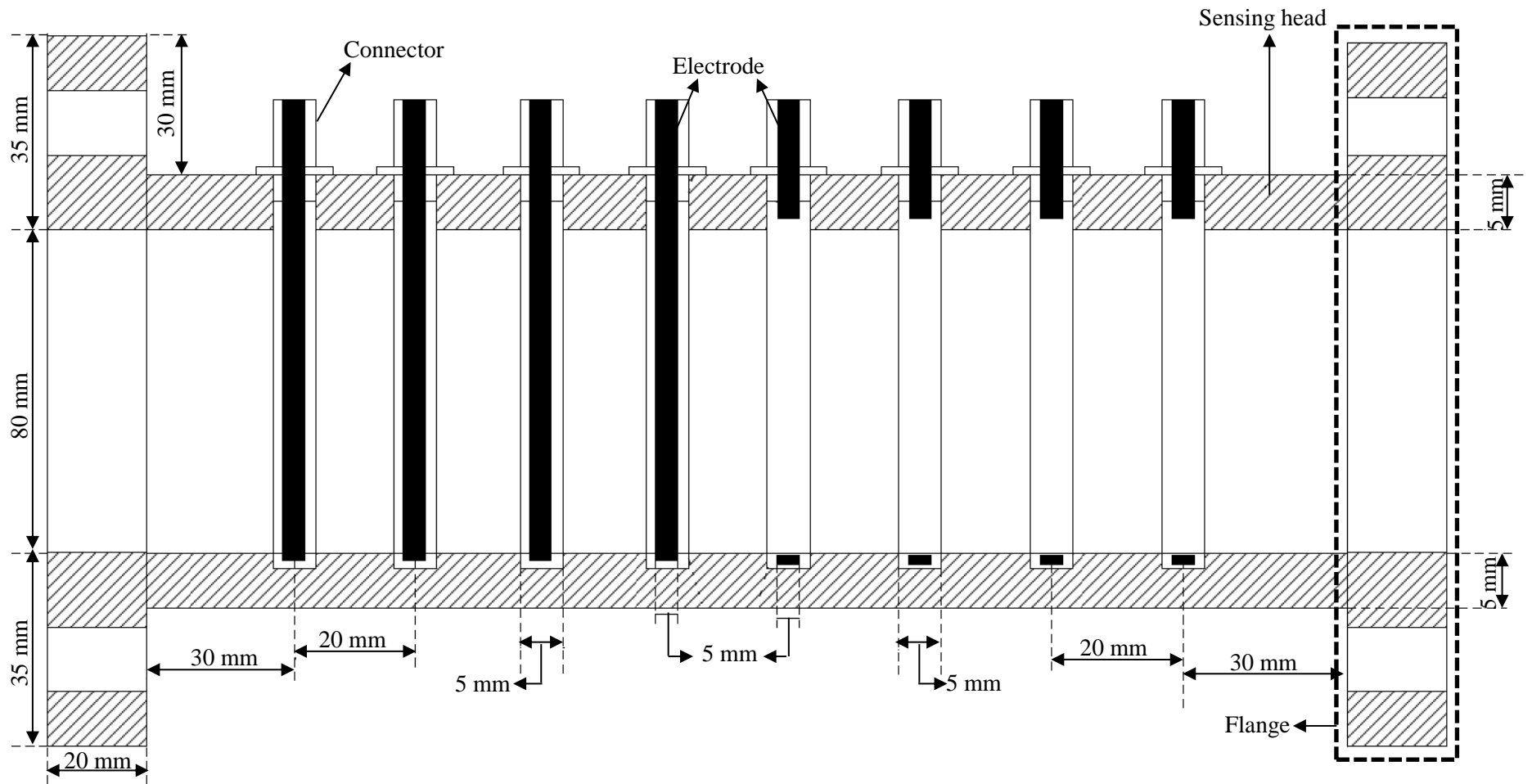


Figure 3.9: Cross-sectional view of the structure of the sensing head

Electrostatic sensing head for velocity measurement on gravity flow rig is shown in Figure 3.10. It used circular-ring electrode consisting of upstream and downstream electrodes and mounted on the gravity flow rig. The whole sensing head is covered with grounded shield to reduce the external electromagnetic interference.

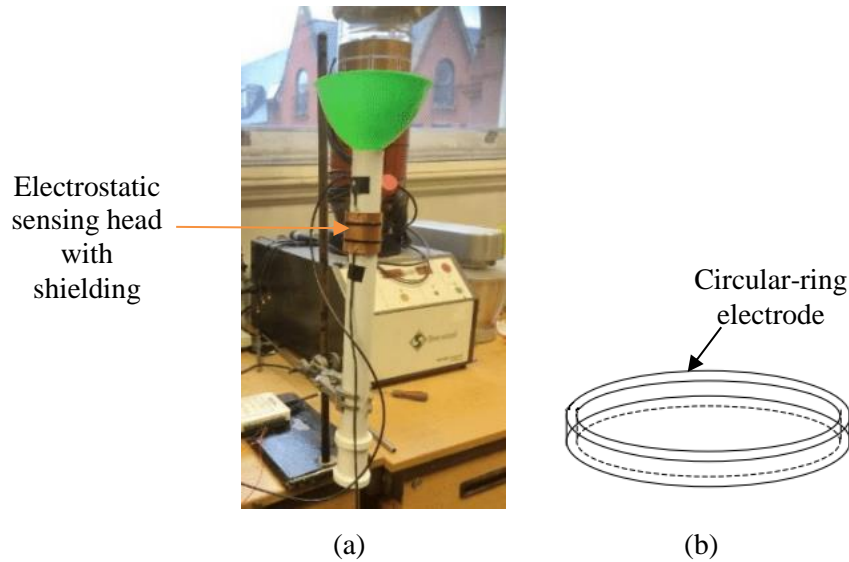


Figure 3.10: (a) Electrostatic sensing head with shielding on gravity flow rig, and (b) the circular-ring shaped electrode of the electrostatic sensor

### 3.3.2 Signal Conditioning Circuit

During handling and transport of granular and powdered materials, electrostatic charge accumulates on the particles. The magnitude of charge depends on many factors such as the physical properties of the particles; including shape, size, density, conductivity, permittivity, humidity and composition (Thuku *et al.*, 2014). The pipe wall roughness, pipe diameter, pipe length traversed by the particles, solids velocity and concentration also are major factors contributing to the magnitude of charge. This electrode charge can be detected using electrodes or plates and converted into a voltage by the signal conditioning circuit. The voltage is amplified by an AC amplifier. The output at this stage is used for cross-correlation measurement.

A complete signal conditioning circuit is shown in Figure 3.11, which consists of charge-to-voltage converter and an amplifier circuit. The input to the charge-to-voltage converter, is the induced charge signal that are collected by the electrodes of the electrostatic sensor. The output of the circuit is a voltage signal and the amount of output voltage is proportional to the amount of input charge. However, the

signals captured by the electrode may include unwanted extrinsic noises which causes the interested output signal is damaged or totally drown by unwanted extrinsic noise. One of the most extrinsic noise problems can be imposed from a 50 Hz or 60 Hz power supply. Hence, high pass filter is employed to weaken the signals with a frequency lower than the cut-off frequency  $f_c$  and passes the signals with a frequency higher than the  $f_c$ . The high pass filter circuit in Figure 3.5 has a cut-off frequency of 15.915 kHz. The signal conditioning circuit deals with a random and a very small range of electric charge fluctuation. Hence, an amplifier circuit with a bandwidth of 450 kHz is utilised to amplify the small output voltage coming from the high pass filter.

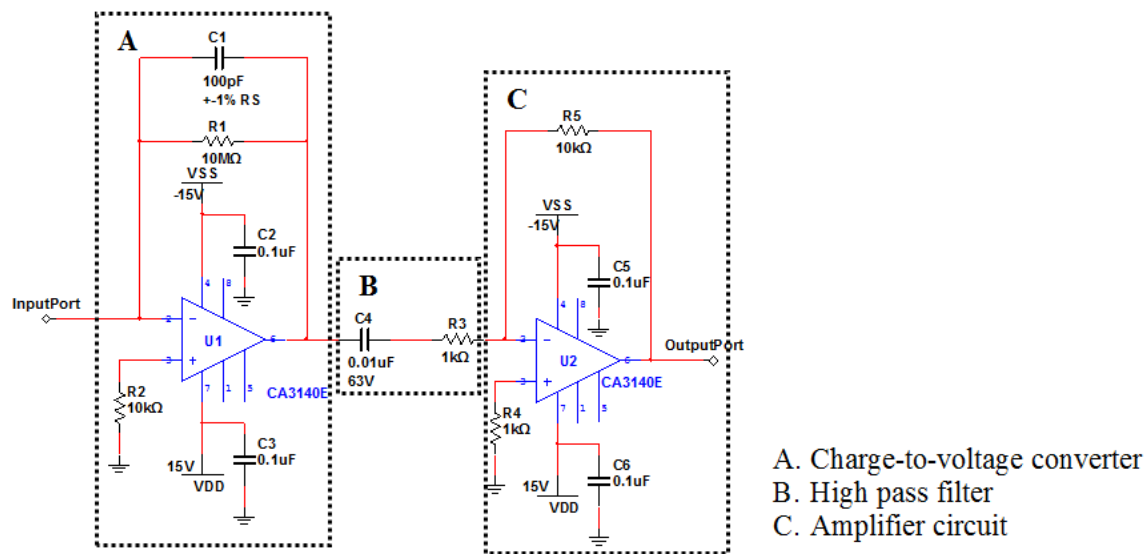


Figure 3.11: Schematic diagram of a signal conditioning circuit

### 3.3.3 Data Acquisition System

A data acquisition (DAQ) system is essential to measure the physical phenomena in a process equipment such as velocity of solids moving in a pneumatic conveyor or material fraction in CFB. A DAQ system is used to acquire, analyse and eventually present the information in a computer. The essential components of DAQ system include sensors, signal conditioning circuitry, DAQ device and a computer. Apart from that, a software is also required to control the data transfer and measurement task. The software also has the ability to support the DAQ device to carry out such tasks.

Figure 3.12 shows a block diagram of a DAQ system. The measurement of solids velocity in a pipeline begins with an electrostatic sensor. The used to collect and convert the charge into electrical signals as well as to amplify the electrical signals. These analogue signals are converted into digital signals by

the DAQ device, which is National Instruments myDAQ (NI myDAQ) in this work. It is a low-cost, portable USB DAQ device. A DAQ device driver is needed for the DAQ hardware to communicate with the computer. The DAQ driver adaptor allows user to interface the DAQ device directly with MATLAB® through Data Acquisition Toolbox. The data acquired from myDAQ is stored in a temporary memory in a data acquisition engine. The data is not automatically available in MATLAB® workspace. They need to be extracted from the data acquisition engine using a MATLAB® function called *s.startForeground*, into MATLAB® workspace for analysis and visualisation. The data in the engine can also be stored permanently in a disk or computer files.

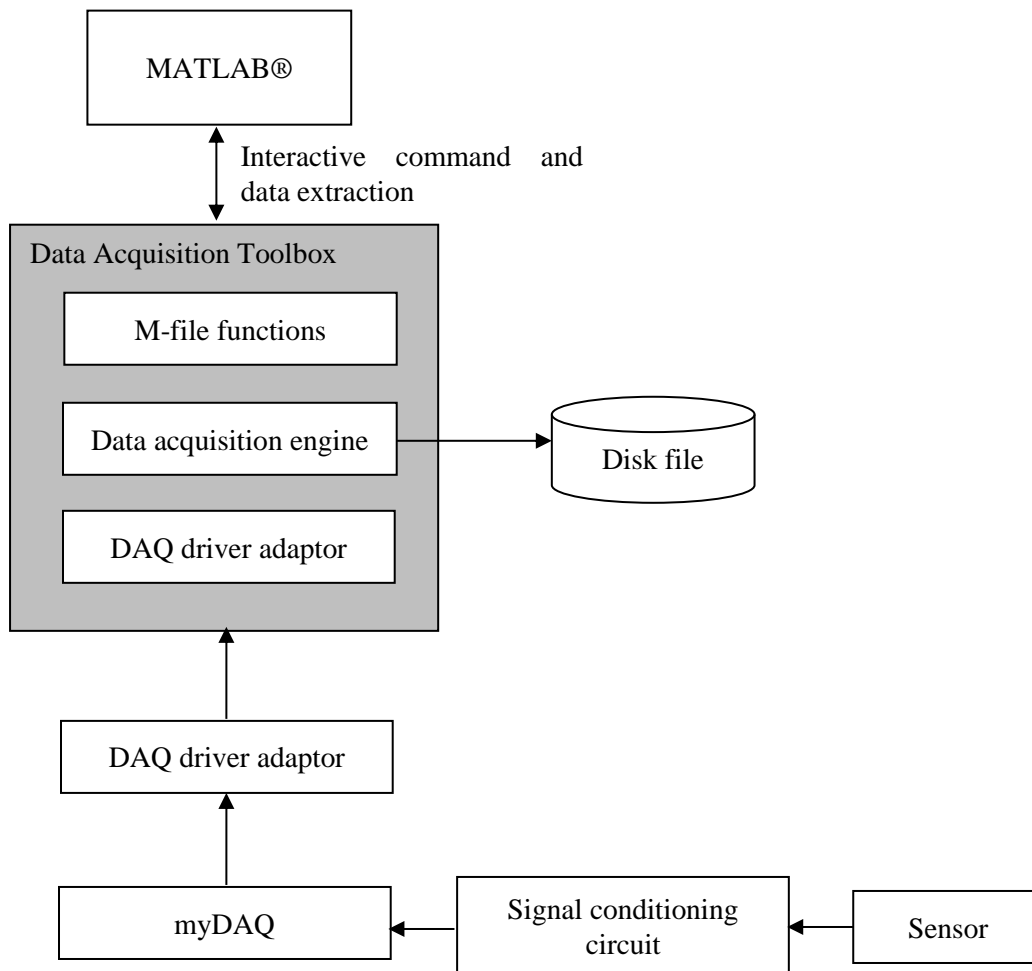


Figure 3.12: Block diagram of a DAQ system for electrostatic sensor

### 3.4 Mass Flow Measurement on Standpipe

The purpose of the work in this sub-section is to measure the mass flow rate of gas/solids flow in a standpipe of a CFB. The discussion about this experiment includes the introduction of CFB, the

conveying materials and fluidisation velocity used, the operation of CFB and the position of the ECT and electrostatic sensor on the standpipe of the CFB.

### **3.4.1 Pilot-plant Scale CFB**

Power stations are one of main causes of industrial pollution to air (Liu et al., 2018a). In some countries, coal is still the main source for generating electricity. For instance, in China 45% electricity is generated by direct burning of coal (Yuan et al., 2018). Coal-fired power stations emit a substantial amount of pollutants such as carbon dioxide, a greenhouse gas responsible for global warming, as well as NO<sub>x</sub>, an acid gas, which affects human health and vegetation. The emissions of pollutants have far-reaching effect and can cause long-range air pollution. As a result, many environmental agencies around the world have forced power stations and industrial facilities to comply with specific emission limit. The agencies may suspend or revoke the licence to operate the facilities if they fail to control the emission of the pollutants. As a result, the demand of cleaner coal combustion systems that has the ability to achieve lower emission of pollutants has increased. One such coal combustion system is circulating fluidised bed (CFB).

The Institute of Engineering Thermophysics, Chinese Academy of Sciences in Beijing, China has developed an air blown pilot-scale CFB system and has been actively carried out various projects in this technology (Liu et al., 2018b; Ouyang et al., 2018; Zhu et al., in press; Liang et al., in press). In fact, the experiment is focusing on measuring the mass flow rate of gas/solids flows in a standpipe which is one of the parts of CFB. The schematic diagram of a CFB system and the experimental setup is shown in Figure 3.13. The CFB system consists of a riser and a solids return system, which consists of a cyclone, a standpipe, a loop seal system and a recycle pipe. The loop seal section of the circulation system is a non-mechanical valve consisting of supply and recycle chambers. The recycle chamber is connected to the lower section of the CFB riser by means of the recycle pipe. The cyclone is made of carbon steel whereas the riser, the standpipe and the loop seal are made from acrylic material.

### **3.4.2 Experimental Setup**

The experiment started by pouring the feed materials in the riser column through a feed port. The feed materials that have been used for this experiment are sand and corn. The material densities and dielectric constants for dry granule corn and sand are shown in Table 3.2. Then, an air compressor supplies the air to the riser column and standpipe. Five fluidisation velocities are utilised for this experiment vary within  $[2 \text{ m s}^{-1}, 10 \text{ m s}^{-1}]$  with  $2 \text{ m s}^{-1}$  interval. The air is distributed across the diameter of the riser, which fluidises the bed material. During the fluidisation, the coarser particles are extracted continuously

from the bottom of the fluidiser whereas the fines along with air travel upward and are separated in the cyclone. The separated air is released to the atmosphere whereas the fine material is accumulated in the standpipe and travel downward. The fine material is fed back to the riser through the loop seal connected to the recycle pipe.

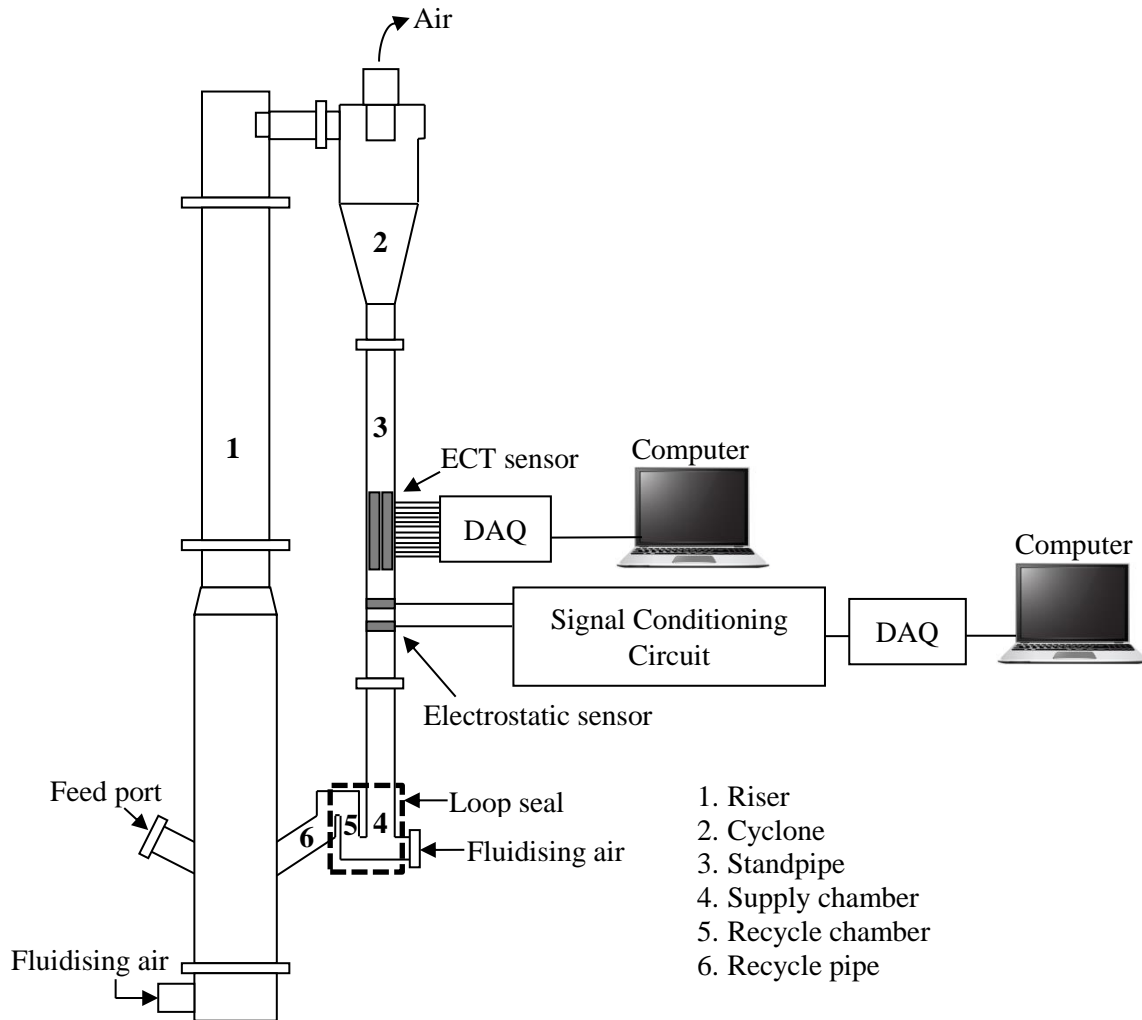


Figure 3.13: Schematic diagram of the test facility of circulating fluidised bed (CFB)

Table 3.2: Material densities and dielectric constants for sand and corn

Material	Material Density (kg/m <sup>3</sup> )	Dielectric constant
Corn (Dry granule)	641	1.8
Sand	1281	4

A 12-electrode ECT sensor and an electrostatic sensor are attached on the standpipe to measure the solids concentration and solids velocity, respectively. Then, ECT data are used to develop the ECT



images and calculate the solids concentrations. In this experiment, the ECT sensor is set to capture 60 frame per minute for each measurement. Meanwhile, output signals from electrostatic sensor are used to calculate the solids velocity using cross-correlation technique.

### **3.5 Mass Flow Measurement on Gravity Flow Rig**

Multi-modal sensor consisting of ECT and electrostatic sensors are also utilised for measuring the mass of material in gravity flow rig. Two sets of electrostatic sensor are used to deal with velocity before and after the ECT sensor. The procedures to develop these electrostatic sensors involved determining the optimised electrode length and distance between upstream and downstream electrodes. Next, the optimised electrode length and distance are used to build two sets of electrostatic sensor. These electrostatic sensors along with an ECT sensor mounted between them (see Figure 3.2 in sub-section 3.1) are then, used to measure the solids velocity and solids concentration, respectively. It is easier to develop this mass flow measurement system using gravity flow rig because it is smaller and easy to handle compared to CFB.

#### **3.5.1 Optimising Electrode Length and Distance of Electrostatic Sensor**

Before an 8-electrode ECT and electrostatic sensors are used to measure the mass of material in a gravity flow rig, the optimum electrode length and distance between upstream and downstream electrodes are first determined. Initially, an 8-electrode ECT sensor is positioned and mounted on a gravity flow rig which is 71.4 cm from the opening of the gravity flow rig to the centre of the ECT sensor as shown in Figure 3.14. The investigation for optimum electrode length and distance is performed by placing the upstream and downstream electrodes beneath the ECT sensor with a distance of 10.7 cm from the sensor ECT. Circular-ring electrode is used to build the electrostatic sensor and the electrode length and distance between the upstream and downstream electrodes are varied. In this work, five different distances between upstream and downstream electrodes are investigated vary from 2 cm until 10 cm with 2 cm interval. Also, five different electrode lengths are also used ranging from 2 mm until 10 mm with 2 mm interval.

In the beginning, electrostatic sensor with an electrode length of 2 mm and a distance of 2 cm between the upstream and downstream electrodes are is mounted on the gravity flow rig as show in Figure 3.14. The solid particles used are plastic beads with an average size of 3 mm, which fall from the funnel on top due to gravitational force. The experiment is begun by pouring the plastic beads into the funnel, the material is streaming down the rig and the outputs from the electrostatic sensor are recorded. Next, the electrodes are fixed with the same electrode length of 2 mm and the distance between the electrodes are

changed to 4 cm. Plastic beads is poured again into the funnel and the outputs from the electrostatic sensor are recorded. Experiments are repeated with the distances between upstream and downstream electrodes of 6 cm, 8 cm and 10 cm. After that, the electrode length is changed to 4 mm and the experiments are repeated for the distances of 2 cm until 10 cm with 2 cm interval. The experiments are continued for the electrode lengths of 6 mm, 8 mm and 10 mm with various distance of 2 cm until 10 cm with 2 cm interval. All the outputs from electrostatic sensor are used to calculate the correlation velocity using equations (2.20) and (2.21) from sub-section 2.31.

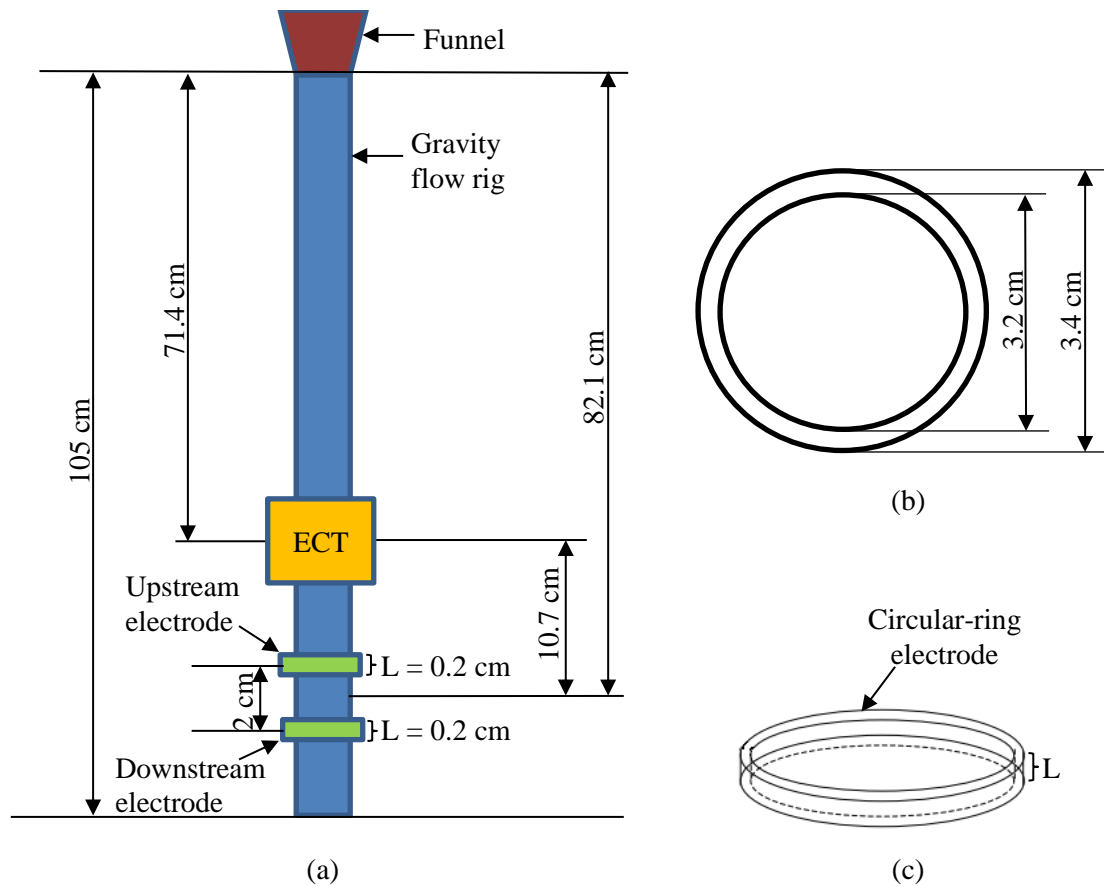


Figure 3.14: Schematic diagram of gravity flow rig used to investigate the optimisation of electrode length and distance between upstream and downstream electrodes, (b) the cross-sectional area of the gravity flow rig and (c) the circular-ring shaped electrode of the electrostatic sensor

### 3.5.2 Assessing the Performance of Optimised Electrode Length and Distance

The selection of optimum electrode length and distance is based on the smallest error between free flow velocity and correlation velocity for all electrode lengths and distances. Before the free flow velocity is calculated, the distance electrostatic sensor from the opening of the pipe to the centre of the pipe is

measured. This distance from the opening of the rig to the centre of the electrostatic sensor is different for each electrode length and distance as shown in Table 3.3.

Table 3.3: Height (in m) from the opening of the gravity flow rig to the centre of electrostatic sensor

Electrode length, L	Distance between upstream and downstream electrodes, $d$				
	2 cm	4 cm	6 cm	8 cm	10 cm
2 mm	0.821 m	0.831 m	0.841 m	0.851 m	0.861 m
4 mm	0.822 m	0.832 m	0.842 m	0.852 m	0.862 m
6 mm	0.823 m	0.833 m	0.843 m	0.853 m	0.863 m
8 mm	0.824 m	0.834 m	0.844 m	0.854 m	0.864 m
10 mm	0.825 m	0.835 m	0.845 m	0.855 m	0.865 m

Subsequently, the free flow velocity is calculated for each distance shown in Table 3.3 using

$$v_{free\_flow} = \sqrt{2gH} \quad (3.1)$$

where  $g$  is the acceleration due to gravity and  $H$  is the height from the opening of the gravity flow rig to the centre of the sensor. Finally, the absolute error percentage for each electrode length and distance can be calculated using

$$Absolute\ error = \frac{|Experimental\ value - Reference\ value|}{Reference\ value} \times 100\% \quad (3.2)$$

where in this case, experimental value is the correlation velocity and the reference value is the free fall velocity. The optimum electrode length and distance is chosen based on the smallest absolute error.

### 3.5.3 Mass Flow Meter by ECT and Two Sets of Electrostatic Sensor

In this work, two sets of electrostatic sensor is mounted at each end of ECT sensor on gravity flow rig as shown in Figure 3.15. The optimum electrode length and distance between upstream and downstream electrodes obtained from experiment in previous sub-section is used to build the two sets of electrostatic sensor. The electrostatic sensor located above ECT sensor is called upper electrostatic sensor and denoted by ES1 where the one located below ECT sensor is called lower electrostatic sensor and denoted as ES2. From the figure, it can be seen that both electrostatic sensors are mounted with a distance of 15.1 cm from the centre of the electrostatic sensor to the centre of the ECT sensor.

Salt with material density of  $2165 \text{ kg m}^{-3}$  and the reference mass of 1 kg is used in this experiment. The experiments are repeated four times and the output signals from the electrostatic sensor and ECT sensor are recorded. Also, in this research ECT sensor captured 2000 frames per 20 seconds for each

measurement. Solids concentration is obtained from the ECT sensor whereas for each set of electrostatic sensor, the solids velocity are calculated using cross-correlation technique as explained in sub-section 2.31.

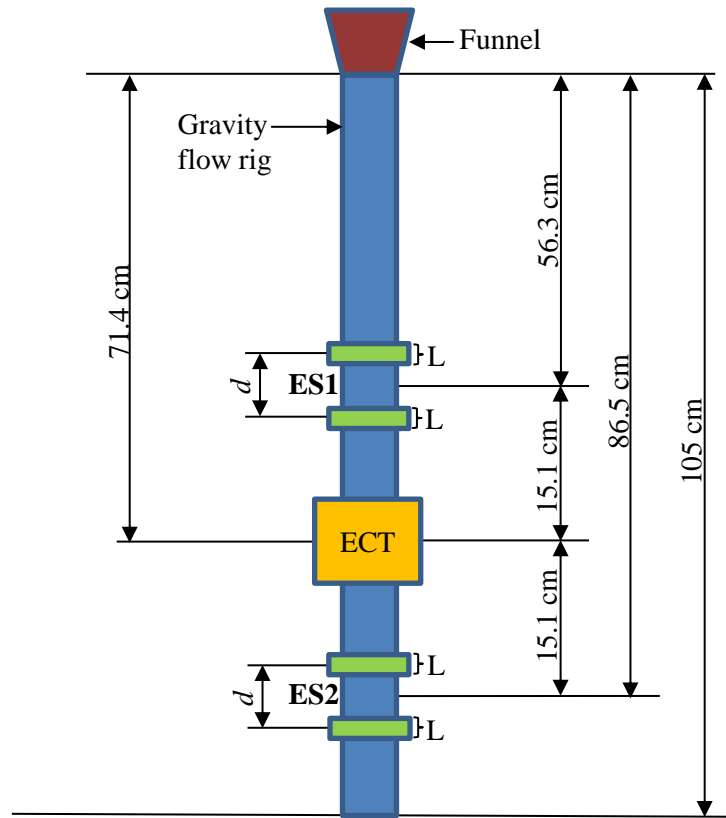


Figure 3.15: Schematic diagram of an ECT sensor and two sets of electrostatic sensor attached on gravity flow rig

### 3.5.4 Solids Velocity Using Two Sets of Electrostatic Sensor

This sub-section aims to obtain the equations to calculate solids velocity using two sets of electrostatic sensor based on the mass flow meter shown in Figure 3.15. Referring to Figure 3.16, the distance from the opening of the pipe to the centre of upper electrostatic sensor ES1 is  $h$ , the centre-to-centre distance of upper electrostatic sensor ES1 and lower electrostatic sensor ES2 is  $D$ , and the distance from the opening of the pipe to the centre of ECT sensor is  $h + \frac{D}{2}$ . Thus, the free fall velocity at ES1 section is  $V_1 = \sqrt{2gh}$ , the free fall velocity at ES2 section is  $V_2 = \sqrt{2g(h + D)}$  and the fall velocity at ECT section is  $V_3 = \sqrt{2g(h + \frac{D}{2})}$ .

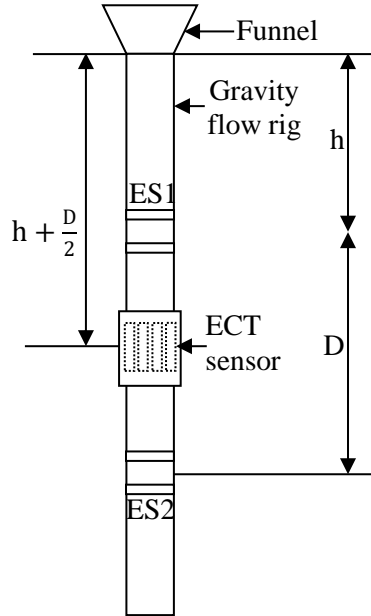


Figure 3.16: Gravity flow rig with an ECT sensor and two sets of electrostatic sensor

Rearranging the free fall velocity at ES1 section,

$$h = \frac{V_1^2}{2g} \quad (3.3)$$

Also, rearranging the free fall velocity at ES2 section,

$$D = \frac{V_2^2 - V_1^2}{2g} \quad (3.4)$$

Substituting equations (3.3) and (3.4) in free fall velocity equation at ECT section,

$$V_3 = \sqrt{\frac{V_2^2 - V_1^2}{2}} \quad (3.5)$$

Eventually, the solids velocity measured using two sets of electrostatic sensor on the gravity flow rig can be calculated from equation (3.5), which is the equation of free fall velocity at ECT section based on the two sets of electrostatic sensor.

### 3.5.5 Mass Flow Calculation and Assessing the Performance of Mass Flow Meter

Solids concentration can be obtained from discussion explained in sub-section 2.3.2 whereas solids velocity for this mass flow meter can be obtained using cross-correlation technique explained in sub-section 2.3.1 as well as from discussion in sub-section 3.5.4. Then, this information is used to calculate the mass of salt using equation (2.19) in sub-section 2.3.

Finally, the mass of salt in this experiment is compared with reference mass of salt which is 1 kg and the performance of the mass flow meter using ECT sensor and two sets of electrostatic sensor is evaluated based on absolute error based on equation (3.2).

## CHAPTER 4

### RESULTS AND DISCUSSION

#### 4.1 Electrostatic Sensor on Standpipe

Figures 4.1 and 4.2 show output signals from electrostatic sensor for dry sand and dry granule corn, respectively, in standpipe at fluidisation velocities of  $2 \text{ m s}^{-1}$  until  $10 \text{ m s}^{-1}$  with  $2 \text{ m s}^{-1}$  interval. As a comparison purpose, an output from electrostatic sensor with an electrode length of 2 mm and distance of 2 cm obtained from experiment in sub-section 3.5 is presented in Figure 4.3. Based on Figure 4.3, it can be seen that output signals from electrostatic sensor are random and has a very small range of fluctuation. However, all the output signals in Figures 4.1 and 4.2 have a very huge amplitude compared to Figure 4.3. This may due to noise that had swamped the electrostatic signals and render the data as useless. The signal conditioning circuit that collects these signals has high amplification properties and the output signals are extremely vulnerable to be damaged by noise. In addition, sensor electrodes are also highly sensitive to noise. An electromagnetic field from an AC power line near the sensor easily can be detected by sensor electrode and amplified by the signal conditioning circuit that can drown and damage the desired signal from the electrostatic charge source. Based on the results in Figures 4.1 and 4.2 also show that there is a lot of electromagnetic noise such as noise from a lot of power lines used in the CFB laboratory and it affect the outputs of the electrostatic sensor. However, it is not known why 50 Hz noise is more prominent in Figure 4.1 compared to in Figure 4.2.

The results of solids velocities are not presented as it is clearly shown that the output signals from electrostatic sensor are unusable for further calculation.

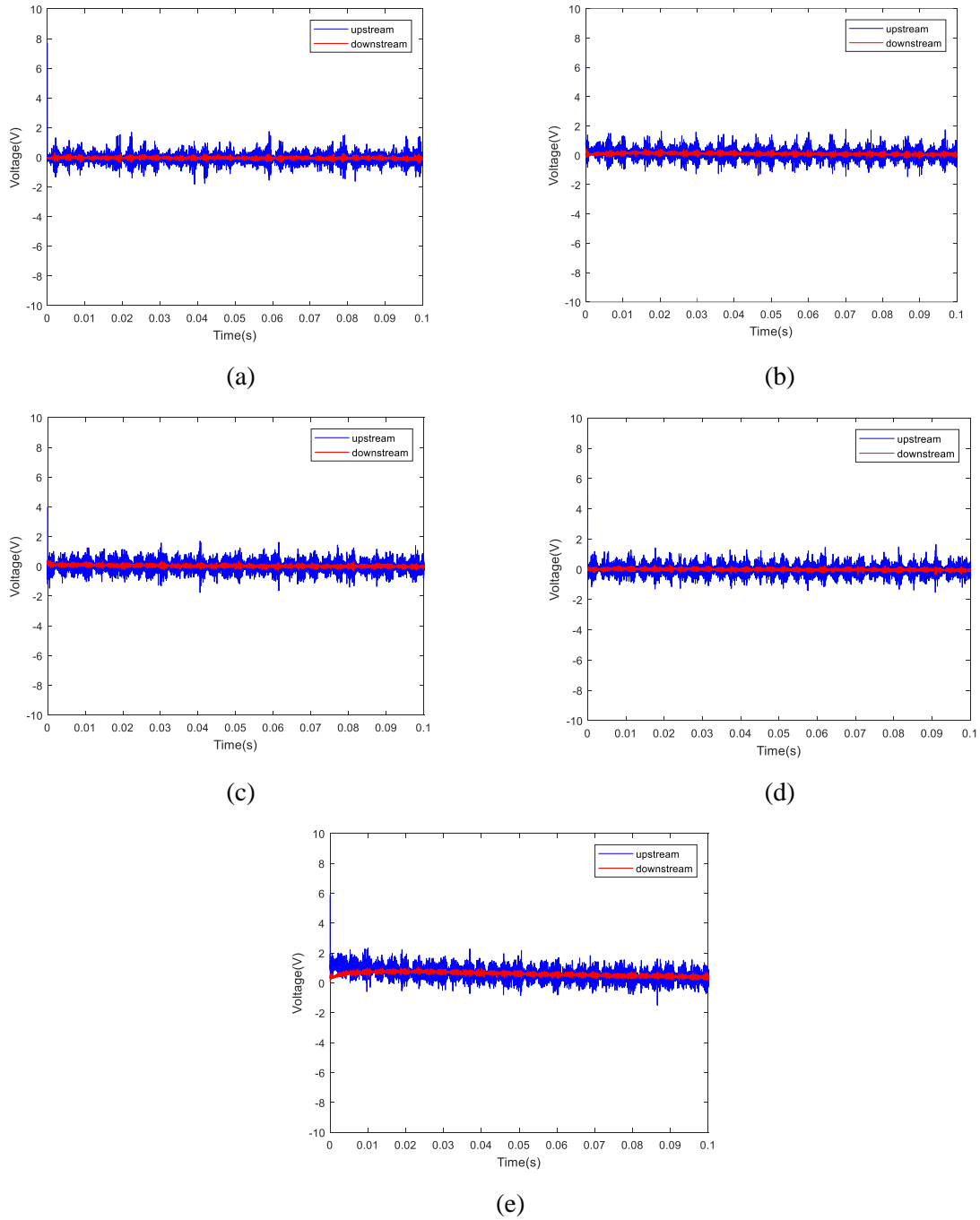
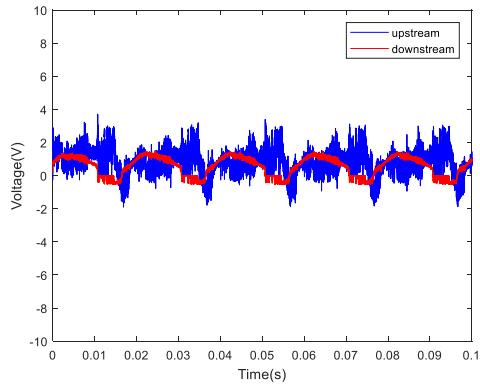
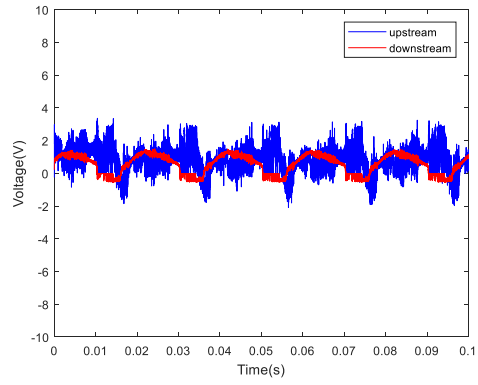


Figure 4.1: Output signals from upstream and downstream electrodes for dry sand at fluidisation velocity of (a)  $2 \text{ m s}^{-1}$ , (b)  $4 \text{ m s}^{-1}$ , (c)  $6 \text{ m s}^{-1}$ , (d)  $8 \text{ m s}^{-1}$  and (e)  $10 \text{ m s}^{-1}$

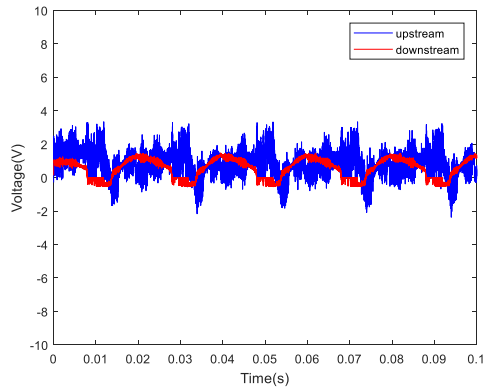




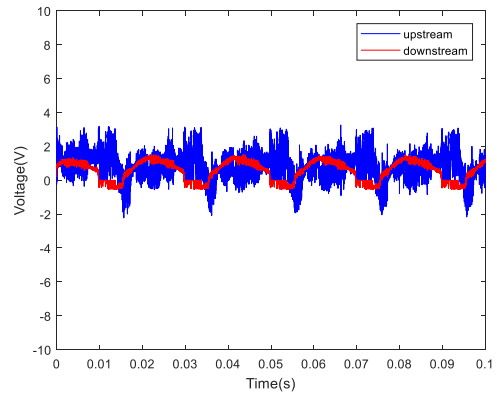
(a)



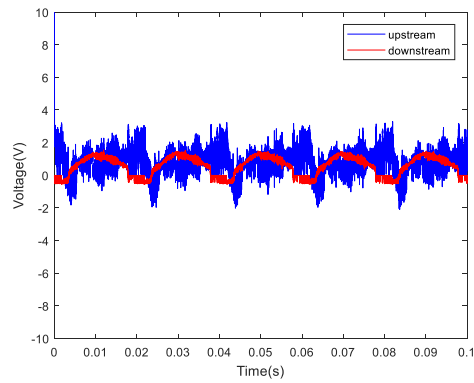
(b)



(c)



(d)



(e)

Figure 4.2: Output signals from upstream and downstream electrodes for dry granule corn at fluidisation velocity of (a)  $2 \text{ m s}^{-1}$ , (b)  $4 \text{ m s}^{-1}$ , (c)  $6 \text{ m s}^{-1}$ , (d)  $8 \text{ m s}^{-1}$  and (e)  $10 \text{ m s}^{-1}$

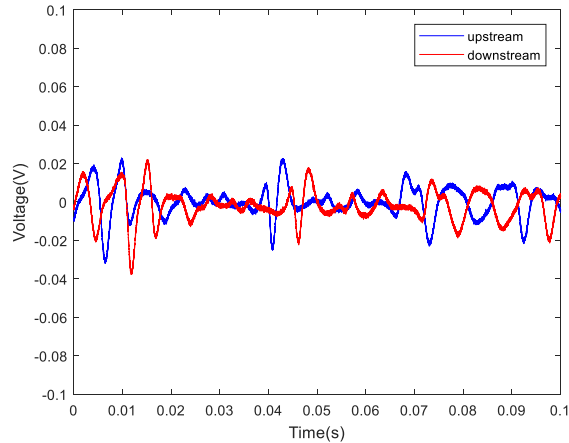


Figure 4.3: Experimental result from sub-section 3.5 conducted using electrostatic sensor with electrode length of 2 mm and distance of 2 cm.

## 4.2 ECT Images of Gas/Solid Flow in a Standpipe

Table 4.1 shows ECT images of gas/solids flows for dry sand in the standpipe with five different fluidisation velocities vary in the range of  $[2 \text{ m s}^{-1}, 10 \text{ m s}^{-1}]$  with  $2 \text{ m s}^{-1}$  interval. The ECT data are obtained simultaneously with the output signals from electrostatic sensor for one minute. The ECT sensor is set to capture 60 frames or one minute. Table 4.1 shows how ECT images of gas/solids flow for dry sand changes from 1<sup>st</sup> second to 60<sup>th</sup> second with 10 seconds interval. The blue region means that the cross-sectional area within the standpipe is filled with air whereas the red region in means that the area is filled with solids material. Based on Table 4.1 it can be seen that the sand material is filled mostly at the centre of the standpipe as well as some of standpipe inner wall, because the measurements are taken at a steady state whereby the material fall from the cyclone through to the centre of the standpipe. Table 4.1 also shows that the concentration of solids at the centre of the pipe increases with the increase in the fluidisation velocity.

Table 4.2 shows ECT images of gas/solids flows for dry granule corn in standpipe with five different fluidisation velocities. It can be seen that corn is concentrated at some edges of the standpipe wall at fluidisation velocity of  $2 \text{ ms}^{-1}$  and  $4 \text{ ms}^{-1}$ . At fluidisation of  $6 \text{ ms}^{-1}$ , the ECT images show the corn initially concentrated in the centre of the pipe and it concentrated at edge of the standpipe inner wall at 10<sup>th</sup> second. The corn filled half of standpipe column at 40<sup>th</sup> second and it concentrated at two parts of standpipe inner column and finally the gas/solids flows are concentrated near some part of the standpipe inner wall as shown at 60<sup>th</sup> second. At fluidisation velocity of  $8 \text{ ms}^{-1}$  the gas/solids flows initially concentrated at some part of standpipe inner column and the concentration increased towards the centre of the standpipe with time. Finally, Table 4.2 shows gas/solids flows of dry granule corn filled almost

the cross-sectional area of standpipe column at fluidisation velocity of  $10 \text{ ms}^{-1}$ , because the higher fluidisation velocity has caused the material evenly distributed across the cross-sectional area of standpipe column.

In the same way as the results of output signals from electrostatic sensor, no further solids concentration calculation is carried out for both sand and dry granule corn.

Table 4.1: ECT images of gas/solids flow for dry sand in a standpipe with five different fluidisation velocities

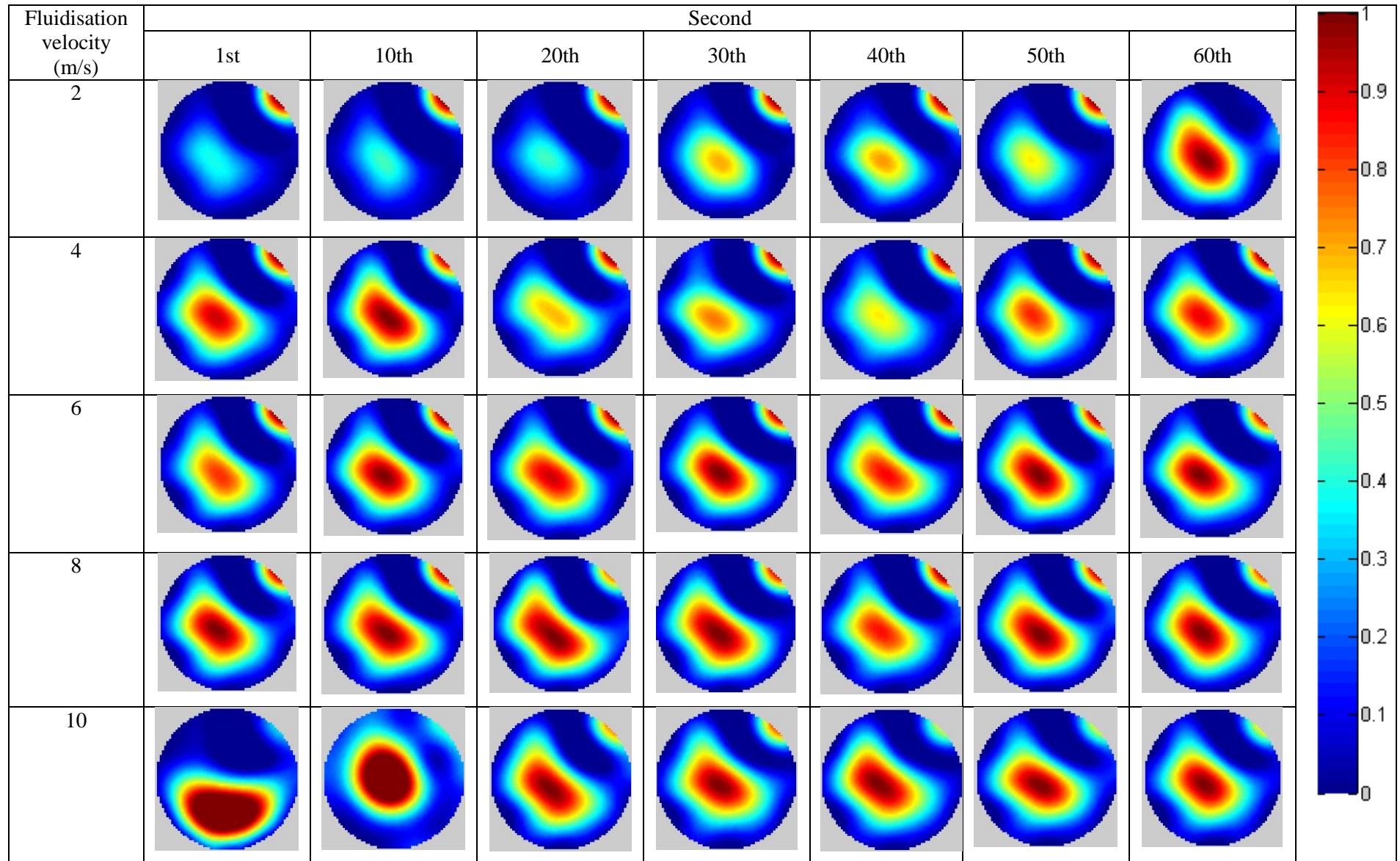
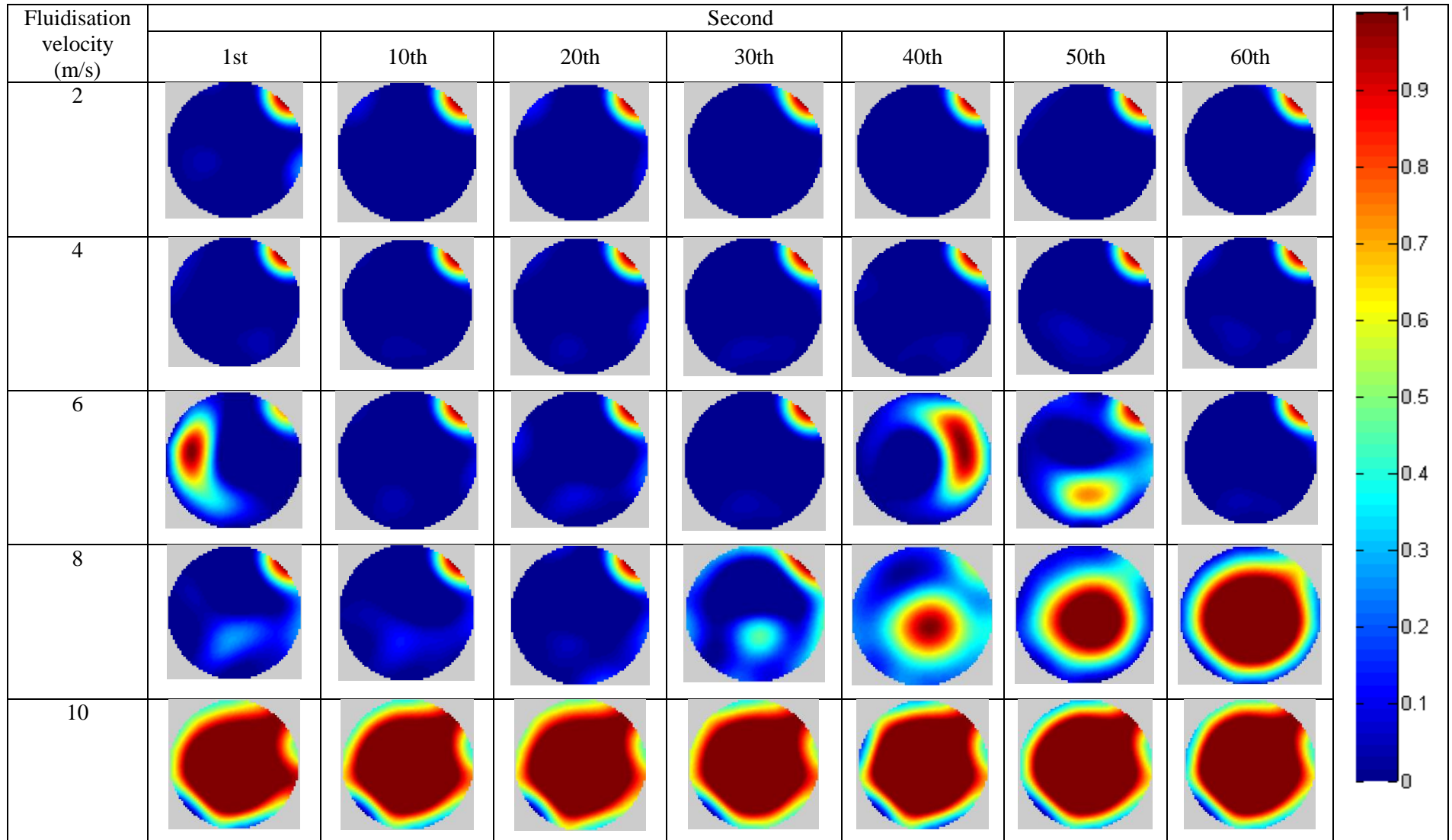


Table 4.2: ECT images of gas/solids flow for dry granule corn in a standpipe with five different fluidisation velocities



### 4.3 Optimised Electrode Length and Distance

This sub-section starts with observation on the outputs of electrostatic sensor and cross-correlation curve for various electrode lengths and distances. The most suitable electrode length and distance of electrostatic sensor for gravity flow rig used in this experiment are also chosen in this sub-section.

Figures 4.4 until 4.8 show the outputs of gas/solids flows and cross correlation curve for gravity flow rig with the length of electrode of 2 mm and various distances between upstream and downstream electrodes. Only outputs of electrostatic sensor and cross-correlation curves with the length of electrode of 2 mm are presented because the procedure to calculate the solids velocity is similar to each other when the cross-correlation technique is used.

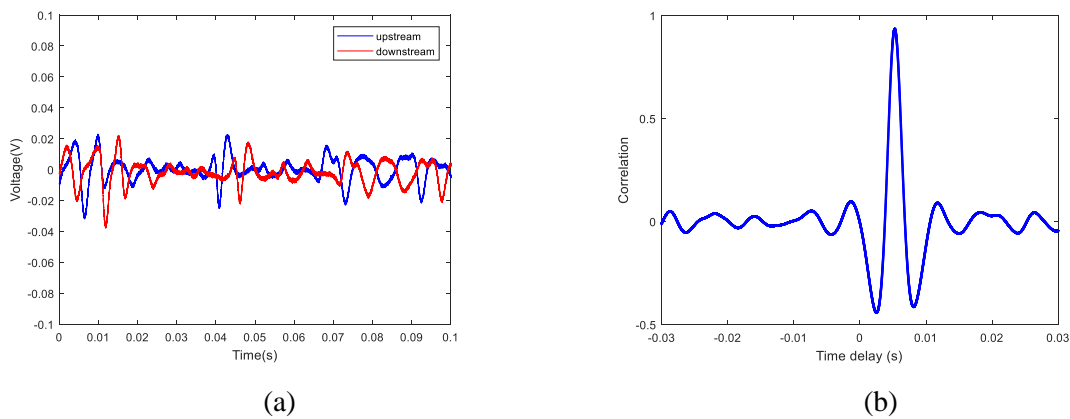


Figure 4.4: (a) Signals from upstream and downstream electrodes and (b) Cross-correlation curve for ring-shaped electrode with length of 2 mm and distance of 2 cm

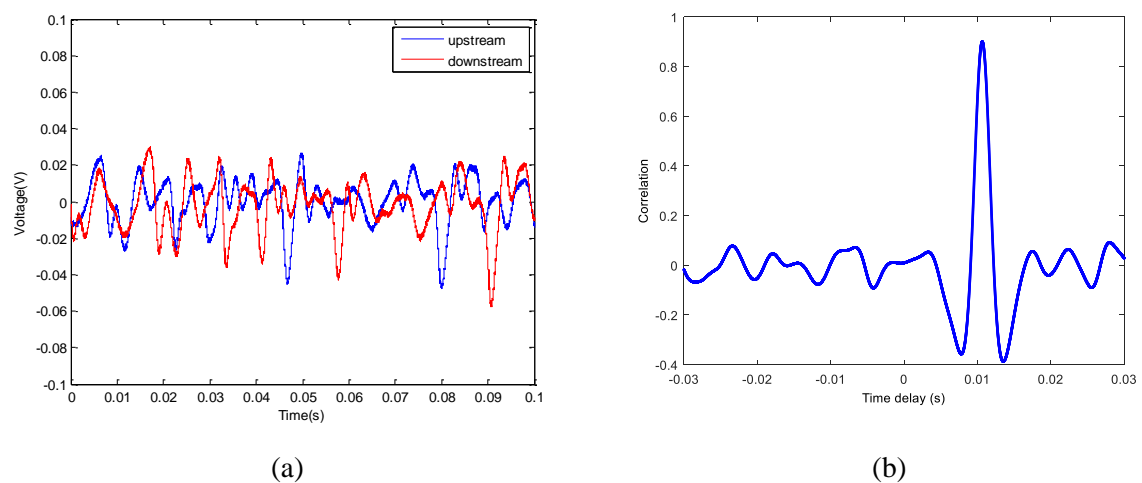
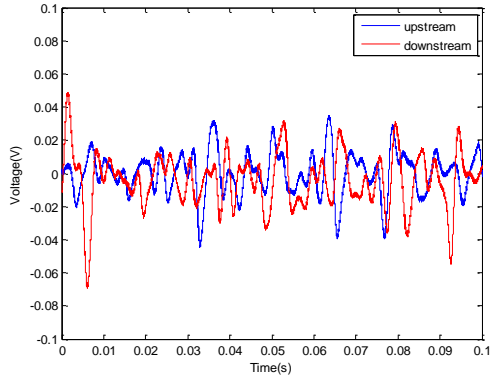
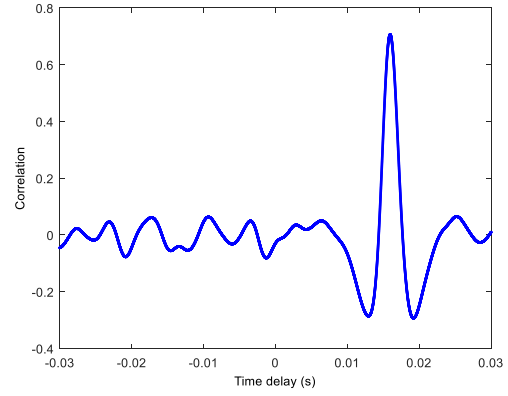


Figure 4.5: (a) Signals from upstream and downstream electrodes and (b) Cross-correlation curve for ring-shaped electrode with length of 2 mm and distance of 4 cm

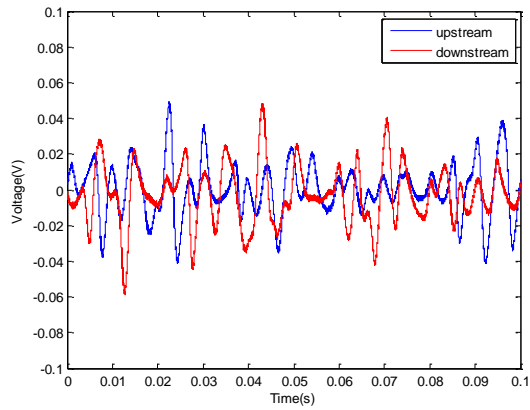


(a)

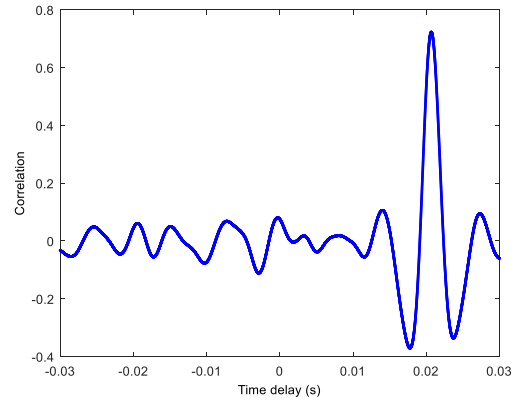


(b)

Figure 4.6: (a) Signals from upstream and downstream electrodes and (b) Cross-correlation curve for ring-shaped electrode with length of 2 mm and distance of 6 cm

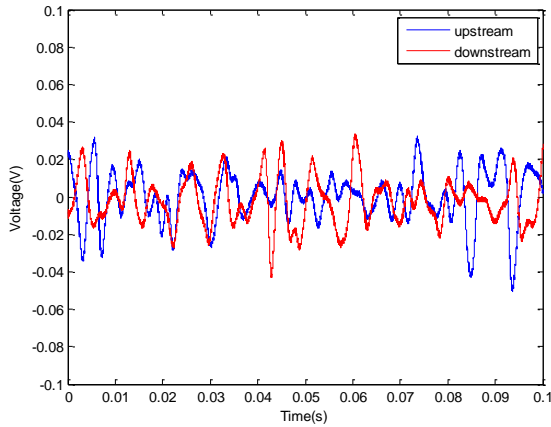


(a)

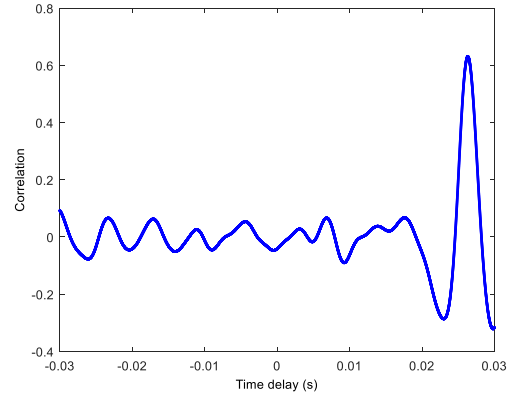


(b)

Figure 4.7: (a) Signals from upstream and downstream electrodes and (b) Cross-correlation curve for ring-shaped electrode with length of 2 mm and distance of 8 cm



(a)



(b)

Figure 4.8: (a) Signals from upstream and downstream electrodes and (b) Cross-correlation curve for ring-shaped electrode with length of 2 mm and distance of 10 cm

Based on Figures 4.4 until 4.8, it can be seen that cross-correlation peak is the highest when the distance between upstream and downstream is 2 cm. The cross-correlation peak decreases as the distance increases. This indicates that the similarity of signals from upstream and downstream electrodes decreases as the distance between the electrodes increases. Tables 4.3 until 4.7 show the correlation peak, time lag and velocity for various electrode lengths and various distances. Based on the tables, it reveals that for all electrode lengths, the time lag increases as the distance increases.

Table 4.3: Experimental results of ring-shaped electrode with length of 2 mm and various distances

Distance (cm)	Correlation peak	Time lag (ms)	Velocity ( $\text{m s}^{-1}$ )
2	0.9345	5.27	3.7951
4	0.9005	10.64	3.7594
6	0.7061	15.95	3.7618
8	0.7223	20.70	3.8657
10	0.6307	26.31	3.8008

Table 4.4: Experimental results of ring-shaped electrode with length of 4 mm and various distances

Distance (cm)	Correlation peak	Time lag (ms)	Velocity ( $\text{m s}^{-1}$ )
2	0.9201	5.40	3.7037
4	0.9263	10.62	3.7665
6	0.8095	16.05	3.7383
8	0.7590	21.27	3.7612
10	0.7167	26.42	3.7850



Table 4.5: Experimental results of ring-shaped electrode with length of 6 mm and various distances

Distance (cm)	Correlation peak	Time lag (ms)	Velocity (m s <sup>-1</sup> )
2	0.9637	5.44	3.6799
4	0.9159	10.81	3.7020
6	0.8764	15.97	3.7570
8	0.7903	21.23	3.7683
10	0.7319	26.67	3.8073

Table 4.6: Experimental results of ring-shaped electrode with length of 8 mm and various distances

Distance (cm)	Correlation peak	Time lag	Velocity (m s <sup>-1</sup> )
2	0.9364	5.47	3.6563
4	0.9402	10.77	3.7157
6	0.8932	15.94	3.7653
8	0.8027	21.23	3.7683
10	0.7588	26.11	3.8300

Table 4.7: Experimental results of ring-shaped electrode with length of 10 mm and various distances

Distance (cm)	Correlation peak	Time lag (ms)	Velocity (m s <sup>-1</sup> )
2	0.9626	5.41	3.6969
4	0.9336	10.63	3.7629
6	0.9226	15.89	3.7771
8	0.8751	20.91	3.8259
10	0.8429	26.00	3.8462

Meanwhile, Table 4.8 shows free fall velocity for various electrode lengths and various distances. Based on the table, as the distance increases, the free fall velocity also increases. When distance between upstream and downstream increases, the height from the opening of the gravity flow rig to the centre of the electrostatic sensor is also increased. Hence, it causes the value of free fall velocity to increase. These heights from the opening of the gravity flow rig to the centre of the electrostatic sensor for various distances are shown in Table 3.3 in sub-section 3.5.2.

Table 4.8: Free fall velocity (in m s<sup>-1</sup>) for various electrode lengths and various distances between upstream and down-stream electrode

Electrode length, L (mm)	Distance between upstream and downstream electrodes, <i>d</i> (cm)				
	2	4	6	8	10
2	4.0128	4.0372	4.0613	4.0855	4.1094
4	4.0152	4.0396	4.0638	4.0879	4.1118
6	4.0177	4.0420	4.0662	4.0903	4.1142
8	4.0201	4.0444	4.0686	4.0927	4.1165
10	4.0226	4.0468	4.0710	4.0950	4.1189

Next, Table 4.9 shows absolute error for various electrode length and various distances between upstream and downstream electrodes. The results in this table suggest that 2 mm is the optimum electrode length and 8 cm is the optimum distance between upstream and downstream electrodes as these values give the least absolute error which is 5.38%. The optimum value of this electrode length

and distance are then used to build two sets of electrostatic sensor mounted above and below the ECT sensor.

Table 4.9: Absolute error (%) for various electrode length and various distances between up-stream and down-stream electrodes

Electrode length, L (mm)	Distance between upstream and downstream electrodes, $d$ (cm)				
	2	4	6	8	10
2	5.43	6.88	7.37	5.38	7.51
4	7.76	6.76	8.01	7.99	7.95
6	8.41	8.41	7.60	7.87	7.46
8	9.05	8.13	7.45	7.93	6.96
10	8.10	7.02	7.22	6.57	6.62

#### 4.4 Solids Velocity Measurement Using Two Sets of Electrostatic Sensor

This sub-section aims to discuss the results of solids velocity measured using upper electrostatic sensor ES1 and lower electrostatic sensor ES2 as well as correlation velocity at ECT section  $V_3$  calculated using equation (3.5) as illustrated in Table 4.10. From the table, it can be seen that the time lag for ES1 is higher than ES2 for all measurements. Experiment also found that the solids velocity for ES2 was greater than ES1 for all measurements. The reason that when the solids streaming down the gravity flow rig, the particle velocity increased and caused the time taken for the particles through the upstream electrode to the downstream electrode of ES2 is smaller than ES1. The values of  $V_3$  for all measurements are then used to calculate the mass of salt later on.

Table 4.10: Experimental results of two sets of electrostatic sensor, ES1 and ES2, and correlation velocity at ECT section

Measurement	ES Sensor	Time lag (ms)	Correlation Velocity ( $\text{m s}^{-1}$ )	Correlation velocity at ECT section $V_3$ ( $\text{m s}^{-1}$ )
First	ES1	25.50	3.1397	3.4389
	ES2	21.50	3.7140	
Second	ES1	25.30	3.1571	3.4675
	ES2	21.30	3.7523	
Third	ES1	25.70	3.1080	3.4282
	ES2	21.50	3.7209	
Fourth	ES1	25.60	3.1299	3.3979
	ES2	21.90	3.6463	

#### 4.5 Mass Flow Calculation and Performance Analysis of Mass Flow Meter

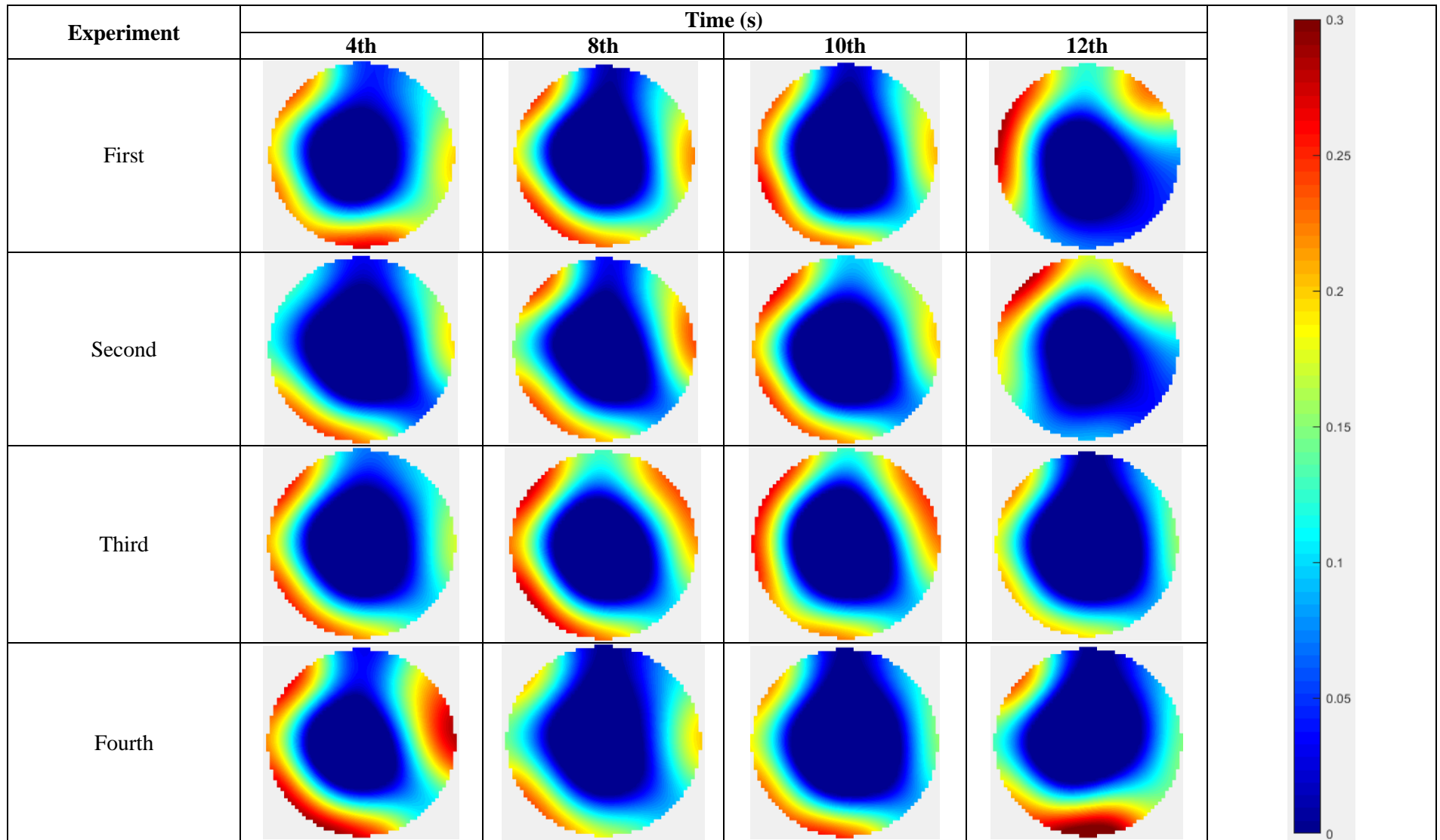
Table 4.11 illustrates mean concentration of salt in gravity rig for all measurements obtained from ECT sensor. The results show a very low concentration around 1.01% until 1.03% which is expected in dilute phase conveying system.

Table 4.11. Mean concentration of salt in gravity flow rig for all measurements

<b>Measurement</b>	<b>Mean concentration (%)</b>
First	1.02
Second	1.01
Third	1.02
Fourth	1.03

Meanwhile, Table 4.12 shows ECT images for gas/solids flow of salt in gravity flow rig. It shows particle flow distribution from fourth second to 12<sup>th</sup> second with 4 seconds interval. . The blue region means that the cross-sectional area within the standpipe is filled with air whereas the red region in means that the area is filled with solids material. Based Table 9 it can be seen that salt is concentrated at the edges of the gravity flow rig wall. The table also shows unsteady flow of salt as some the salt concentrated at different edges of pipe wall at different time. The reason that when salt is poured into the funnel and the salt flow in the rig becomes unstable because the material is poured at different speed every time the measurement is made.

Table 4.12: ECT images for gas/solids flow of salt in gravity flow rig at t=4s until t=12s with 4s interval



Meanwhile, Table 4.13 shows the results of measured mass from the mass flow meter, the reference mass and absolute error for four different measurements. The absolute errors for first, second, third and fourth measurements are 0.75%, 0.47%, 0.33% and 1.22%, respectively. The results obtained from the table are satisfactory as all absolute errors obtained are below 2%. The results suggest that it is feasible to develop a mass flow meter based on ECT sensor and two sets of electrostatic sensor.

Table 4.13: Measured mass, reference mass and absolute error for all measurements

<b>Measurement</b>	<b>Measured mass(kg)</b>	<b>Reference mass (kg)</b>	<b>Absolute Error (%)</b>
First	1.0075	1.000	0.75
Second	1.0047	1.000	0.47
Third	0.9967	1.000	0.33
Fourth	1.0122	1.000	1.22

## CHAPTER 5

### CONCLUSIONS AND SUGGESTION FOR FUTURE WORK

#### 5.1 Conclusions

This research proposes the development of an integrated Electrical Capacitance Tomography (ECT) and electrostatic sensor assembly for mass flow rate measurement of gas/solids flows. Details of the system implementation and development have been described in Chapter 3. Their results have been presented and discussed in Chapter 4.

A standpipe of a circulating fluidised bed (CFB) and a gravity flow rig are two process equipments that involved in measuring the mass flow using the mass flow meter based on ECT and electrostatic sensors. For standpipe, the mass flow meter is build using 12-electrode ECT sensor and an electrostatic sensor mounted beneath the ECT sensor. Meanwhile, 8-electrode ECT sensor mounted between two sets of electrostatic sensor are built to measure the mass flow in a gravity flow rig. Developing two sets of electrostatic sensor involved optimising the electrode length and distance between upstream and downstream electrodes. The electrode length and distance between upstream and downstream electrode of electrostatic sensor are important parameters to be considered as they can affect the output signals. The optimised electrode length and distance between upstream and downstream electrodes are chosen based on the least absolute error calculated and compared using the correlation velocity and free fall velocity, for various electrode lengths and distances. From the results, the optimum electrode length is 2 mm where the optimum distance between upstream and downstream electrode is 8 cm.

In this work, the mass flow measurement on standpipe of CFB cannot be resolved due to the output of electrostatic sensor that have been swamped by noise. However, ECT images have successful been reconstructed using linear back projection (LBP) algorithm.

The mass flow meter based on an ECT sensor and two sets of electrostatic sensor has been successfully developed on a gravity flow rig. The correlation velocity obtained from the two sets of electrostatic sensor are used to calculate the mass of salt. Solids concentration attained from ECT sensor give a very low concentration between 1.01% and 1.03% which is expected in lean phase of gas/solids flows. The absolute errors of mass of salt for four measurement are 0.75%, 0.47%, 0.33% and 1.22%. These very small absolute errors show that the mass flow meter based on an ECT sensor and two sets of electrostatic sensor are able to measure the mass of particle flow in the gravity flow rig. The results demonstrate that it is feasible to develop the mass flow meter based on ECT sensor and two sets of electrostatic sensor.

## **5.2 Suggestion for Future Works**

Based on the findings of this research, a number of possible opportunities can be explored to further enhance the present work. These are outlined below:

- 1) Study the use of electrostatic sensor for gas/solids flows that move upwards and downwards or to the left and to the right, simultaneously. Decoupling these two way movements is necessary so that solids velocity for each way can be determined.
- 2) Considering using the integrated ECT sensor and electrostatic sensor for solids deposition detection on a pipe wall.
- 3) Considering using the integrated ECT sensor and electrostatic sensor to determine moisture content in powder flows.

## REFERENCES

- Abdulkareem, L. A., Azzopardi, B. J., Hamid, S. A. and Abdulkahdir, M. (2015). Characterization of oil/gas flow pattern in vertical pipes using Electrical Capacitance Tomography, *Eur J Sci Res*, 130(1), pp. 160-168.
- Alme, K. J. and Mylvaganam, S. (2006). Electrical capacitance tomography - sensor models, design, simulations, and experimental verification, *IEEE Sens J*, 6(5), pp. 1256-1266.
- Archibong-Eso, A., Baba, D. Y., Aliyu, A., Okeke, N and Giwa, A. (2018). Experimental study of high liquid viscosity oil-gas flows using ECT and gamma radiation methods, *Pet Coal*, 60(2), pp. 196-209.
- Banasiak, R., Wajman, R., Jaworski, T., Fiderek, P., Fidos, H., Nawakowski, J. and Sankowski, D. (2014). Study on two-phase flow regime visualization and identification using 3D electrical capacitance tomography and fuzzy-logic classification, *Int J Multiph Flow*, 58, pp. 1-14.
- Barbir, O and Mathews, J. (2016). Investigation of the influence of gravity on granular flow using silo centrifuge model, *25th European Young Geotechnical Engineers Conference*, Sibiu, Romania, pp. 1-10.
- Beck, M. S. and Plaskowski, A. (1987). *Cross Correlation Flowmeters, Their Design and Application*, Taylor & Francis: UK.
- Bukhari, S. F. A. and Yang, W. (2006). Multi-interface level sensors and new development in monitoring and control of oil separators, *Sensors*, 6(4), pp. 380–389.
- Carter, R. and Yan Y. (2005). An instrumentation system using combined sensing strategies for online mass flow rate measurement and particle sizing, *IEEE Trans Instrum Meas*, 54 (4), pp. 1433-1437.
- Chandrasekera, T. C., Li, Y., Moody, D., Schnellmann, M. A., Dennis, J. S. and Holland, D. J. (2015). Measurement of bubble sizes in fluidised beds using electrical capacitance tomography, *Chem Eng Sci*, 126, pp. 679-687.
- Chao, W., Jingyu, Z., Wenbin, G., Hongbing, D. and Weiping, W. (2015). Cross-correlation focus method with an electrostatic sensor array for local particle velocity measurement in dilute gas-solid two-phase flow, *Meas Sci Technol*, 26(11), pp. 115301.
- Che, H. Q., Wu, M., Ye, J. M., Yang, W. Q. and Wang, H. G. (2018). Monitoring a lab-scale wurster type fluidized bed process by electrical capacitance tomography, *Flow Meas Instrum*, 62, pp. 223-234.
- Coombes, J. R. and Yan, Y. (2016). Measurement of Velocity and Concentration Profiles of Pneumatically Conveyed Particles Using an Electrostatic Sensor Array, *IEEE Trans Instrum Means*, 65(5), pp. 1139-1148.



- Coulthard, J., Cheng, R., Zhang, J. and Keech, R. P. (2012). Test procedures and signal misinterpretation for electrostatics gassolids flowmeters, *Adv Mat Res*, **58**, pp. 1-5.
- Cui, Z., Yang, C., Sun, B. and Wang, H. (2014). Liquid film thickness estimation using electrical capacitance tomography, *Meas Sci Rev*, **14**(1), pp. 8-15.
- Dhodapkar, S., Solt, P. and Klinzing, G. (2009). Understanding bends in pneumatic conveying systems, *Chem Eng*, **116**(4), pp. 53-60.
- Fasching, G. E. and Smith, N. S. (1991). A capacitive system for three-dimensional imaging of fluidized beds, *Rev Sci Instrum*, **62**, pp. 2243-2251.
- Forster-Turner, R. and Hunt, A. (2015). Mass Flow Measurement of Biofuels using Electrical Capacitance Tomography, *International Flow Measurement Conf 2015: Advances & Developments in Industrial Flow Measurement*, Coventry, UK.
- Gajewski, J. B., Glod, B. J. and Kala, W. S. (1990). Electrostatic method for measuring the two-phase pipe flow parameters, *IEEE T Ind Appl*, **29**(3), pp. 650-655.
- Gajewski, J. B., Kacprzyk, R. and Zuk, J. (1993). Electrostatic, Noncontact, Continuous, and Real-time velocity measurements in pneumatic transport pipes, *In Industry Application Society Annual Meeting, Conference Record of the IEEE*, pp. 1709-1713.
- Gajewski, J. B. (1994). Measuring probes, head, and system for the non-contact, electrostatic measurements of the two-phase flow parameters in pneumatic transport of solids, *J Electrostat*, **32**(3), pp. 297-303.
- Gajewski, J. B. (1996). Monitoring electrostatic flow noise for mass flow and mean velocity measurement in pneumatic transport, *J Electrostat*, **37**(4), pp. 261-276.
- Ghafori, H. and Sharifi, M. (2018). Numerical and experimental study of an innovative design of elbow in the pipe line of a pneumatic conveying system, *Powder Technol*, **331**, pp. 171-178.
- Gut, Z. and Wolanski, P. (2010). Flame Imaging Using 3D Electrical Capacitance Tomography, *Combust Sci and Tech*, **182**(11-12), pp. 1580-1585.
- Hammer, E. A. and Green, R. G. (1983). The spatial filtering effect of capacitance transducer electrode (flow measurement), *J Phys E*, **16**(5), pp. 438-443.
- Heydarianasl, M. and Rahmat, M.F.A. (2014). The effects of distance on velocity measurement for different shapes of electrostatic sensor electrodes, *J Teknol*, **69**(8), pp. 71-80.
- Heydarianasl, M. and Rahmat, M. F. (2017). Optimization of electrostatic sensor electrodes using particle swarm optimization technique swarm optimization technique, *Int J AdvManuf Technol*, **89**, pp. 905-919.
- Hu, Y., Yan, Y., Wang, L. and Qian, X. (2016). Non-contact vibration monitoring of power transmission belts through electrostatic sensing, *IEEE Sens J*, **16**(10), pp. 3541-3550.
- Huang, S. M., Plaskowski, A. B., Xie, C. G. and Beck, M. S. (1988), Capacitance-based tomographic imaging system, *Electron Lett*, **24**, pp. 418-419.

- Isaksen, Ø. (1996). A review of reconstruction techniques for capacitance tomography, *Meas Sci Technol*, **7**(3), pp. 325-337.
- Isaksen, Ø. and Nordtvedt, J. E. (1993). A new reconstruction algorithm for use with capacitance based tomography, *Model Ident Control*, **15**(1), pp. 9-21.
- Jaworski, A. J. and Dyakowski, T. (2001). Application of electrical capacitance tomography for measurement of gas-solids flow characteristics in a pneumatic conveying system, *Meas Sci Technol*, **12**(8), pp. 1109-1119.
- Jaworski, A. J. and Meng, G. (2009). On-line measurement of separation dynamics in primary gas/oil/water separators: Challenges and technical solutions - A review, *J Pet Sci Technol*, **68**(1-2), pp. 47–59.
- Klinzing, G.E., Rizk, F., Marcus, R. and Leung, L.S. (2010). An overview of pneumatic conveying systems and performance, In *Pneumatic Conveying of Solids* (pp. 1-33), Springer, Dordrecht.
- Li, J., Kong, M., Xu, C., Wang, S. and Fan, Y. (2015). An integrated instrumentation system for velocity, concentration and mass flow rate measurement of solid particles based on electrostatic and capacitance sensors, *Sensors*, **15**, pp. 31023-31035.
- Li, J., Xu, C. and Wang, S. (2012). Local particle mean velocity measurement using electrostatic sensor matrix in gas-solid two-phase pipe flow, *Flow Meas Instrum*, **27**, pp. 104-112.
- Li, J., Xu, C. and Wang, S. (2014). Spatial filtering characteristics of electrostatic sensor matrix for local velocity measurement of pneumatically conveyed particles, *Measurement*, **53**, pp. 194-205.
- Li, X., Jaworski, A. J. and Mao, X. (2016). Application of a twin-plane Electrical Capacitance Tomography sensor for characterising bubble behaviour in a gas-solids fluidized bed, In: *Proceedings of World Congress on Engineering 2016*. London, UK.
- Li, X., Jaworski, A. J. and Mao, X. (2018). Bubble size and bubble rise velocity estimation by means of electrical capacitance tomography within gas-solids fluidised beds, *Measurement*, **177**, pp. 226-240.
- Li, J., Kong, M., Xu, C., Wang, S. and Fan, Y. (2015). An integrated instrumentation system for velocity, concentration and mass flow rate measurement of solid particles based on electrostatic and capacitance sensors, *Sensors*, **15**, pp. 31023-31035.
- Li, Y., Yang, W., Xie, C. G., Huang, S., Wu, Z., Tsamakis, D. and Lenn, C. (2013). Gas/oil/water flow measurement by electrical capacitance tomography, *Meas Sci Technol*, **24**, pp. 1-12.
- Liang, C., Lyu, Q., Na, Y. and Wang, X. (in press). Gasification of preheated coal: Experiment and thermodynamic equilibrium calculation, *J Inst Energ*, <https://doi.org/10.1016/j.joei.2018.07.006>.
- Liu, J., Liu, S., Liu, Y., Schlaberg, H. I. and Lei, J. (2015). Study of Flame Characteristics Using Electric Capacitance Tomography, *Energy Procedia*, **66**, pp. 229-232.

- Liu, S., Hua, S., Wang, K., Qiu, P., Liu, H., Wu, B., Shao, P., Liu, X., Wu, Y., Xue, Y., Hao, Y. and Tian, H. (2018a). Spatial-temporal variation characteristics of air pollution in Henan of China: Localized emission inventory, WRF/Chem simulations and potential source contribution analysis, *Sci Total Environ*, **624**, pp. 396-406.
- Liu, W., Ouyang, Z., Cao, X. and Na, Y. (2018b). Experimental Research on Flameless Combustion with Coal Preheating Technology, *Energ Fuel*, **32**(6), pp. 7132-7141.
- Ma, J. and Yan, Y. (2000). Design and evaluation of electrostatic sensors for the measurement of velocity of pneumatically conveyed solids, *Flow Meas Instrum*, **11**(3), pp. 195-204.
- Makkawi and Ocone (2007). Integration of ECT measurements with hydrodynamic modelling of conventional gas-solid bubbling bed, *Chem Eng Sci*, **62**(16), pp. 4304-4315.
- Marashdeh, Q., Fan, L.-S., Du, B. and Warsito, W. (2008). Electrical capacitance tomography – a perspective, *Ind Eng Chem Res*, **47**(10), pp. 3708-3719.
- Mohamad, E. J., Marwah, O. M. F., Rahim, R. A., Rahiman, M. H. F. and Muji, S. Z. M. (2011). Electronic design for portable electrical capacitance sensor: A multiphase flow measurement, *4th International Conference on Mechatronics (ICOM)*, Kuala Lumpur, Malaysia, pp. 1-8.
- O'Banion, T. (2013). Coriolis: The direct approach to mass flow measurement, *Chem Eng Prog*, **109**(3), pp. 41-46.
- Olmos, A.M., Primicia, J.A. and Marron, J.L. (2006). Influence of shielding arrangement on ECT sensors, *Sensors*, **6**(9), pp. 1118-1127.
- Omar, R., Hewakandamby, B., Azzi, A. and Azzopardi, B. (2018). Fluid structure behaviour in gas-oil two-phase flow in a moderately large diameter vertical pipe, *Chem Eng Sci*, **187**, pp. 377-390.
- Ouyang, Z., Liu, W., Man, C., Zhu, J. and Liu, J. (2018). Experimental study on combustion, flame and NOX emission of pulverized coal preheated by a preheating burner, *Fuel Process Technol*, **179**, pp. 197-202.
- Peng, L. H., Mou, C. H., Yao, D. Y., Zhang, B. F. and Xiao, D. Y. (2005). Determination of the optimal axial length of the electrode in an electrical capacitance tomography sensor, *Flow Meas Instrum*, **16**, pp. 169-175.
- Qian, X., Yan, Y., Shao, J., Wang, L., Zhou, H. and Wang, C. (2012). Quantitative characterization of pulverized coal and biomass-coal blends in pneumatic conveying pipelines using electrostatic sensor arrays and data fusion techniques, *Meas Sci Technol*, **23**(8), pp. 085307.
- Qian, X., Huang, X., Hu, Y. and Yan, Y. (2014). Pulverized coal flow metering on a full-scale power plant using electrostatic sensor arrays, *Flow Meas Instrum*, **40**, pp. 185-191.
- Qian, X., Yan, Y., Huang, X. and Hu, Y. (2017). Measurement of the Mass Flow and Velocity Distributions of Pulverized Fuel in Primary Air Pipes Using Electrostatic Sensing Techniques, *IEEE Trans Instrum Means*, **66**(5), pp. 944-952.

- Rahmat, M. F. A., Isa, M. D., Rahim, R. A. and Hussin, T. A. R. (2009). Electrodynamics Sensor for the Image Reconstruction Process in an Electrical Charge Tomography System, *Sensors*, **9**, pp. 10291-10308.
- Rautenbach Ch., Melaaen M.C., Halvorsen B.M., 2013. Statistical diagnosis of a gas-solid fluidized bed using Electrical Capacitance Tomography, *Int. J. Multiph Flow*, **49**, pp. 70-77.
- Rodrigues, S. J. and Yong, Y. (2012). A comparative study of rounded and strip electrostatic sensors for non-contact measurement of cable speed, *2012 IEEE International Instrumentation and Measurement Technology Conference (I2MTC)*, Graz, Austria, pp. 1159-1162.
- Saoud, A., Mosorov, V. and Grudzien, K. (2017). Measurement of velocity of gas/solid swirl flow using Electrical Capacitance Tomography and cross-correlation technique, *Flow Meas Instrum*, **53**, pp. 133-140.
- Sardeshpande, M. V., Harinarayan, S. and Ranade, V. V. (2015). Void fraction measurement using electrical capacitance tomography and high speed photography, *Chem Eng Res Des*, **94**, pp. 1-11.
- Sun, M., Liu, S., Lei, J. and Li, Z. (2008). Mass flow measurement of pneumatically conveyed solids using electrical capacitance tomography, *Meas Sci Technol*, **19** (4), pp. 1-6.
- Tajdari, T., Rahmat, M. F. and Wahab, N. A. (2014). New technique to measure particle size using electrostatic sensor, *J Electrostat*, **72**(2), pp. 120-128.
- Thuku, I. T., Rahmat, M. F., Wahab, N. A and Tajdari, T. (2014). Determination of Concentration Profile for Flowing Solid Particles in Pipeline Using Electric Charge Tomography System, *Math Probl Eng*, **2014**, pp. 1-18.
- Tombs, M., Zhou, F. and Henry, M. (2018). Two-phase coriolis mass flow metering with high viscosity oil, *Flow Meas Instrum*, **59**, pp. 23-27.
- Tripathi, N. M., Levy, A. and Kalman, H. (2018). Acceleration pressure drop analysis in horizontal dilute phase pneumatic conveying system, *Powder Technol*, **327**, pp. 43-56.
- Wang, S.J., Dyakowski, T., Xie, C.G., Williams, R.A. and Beck, M.S. (1995). Real time capacitance imaging of bubble formation at the distributor of a fluidized bed, *Chem Eng J Biochem Eng J*, **56**(3), pp.95-100.
- Wang, X., Hu, Y., Qian, X., Wang, L. and Yan, Y. (2014). Non-contact strip speed measurement using an electrostatic sensor array and data fusion technique, *2014 12th International Conference on Signal Processing (ICSP)*, pp. 363-367.
- Wang, X. X., Hu, H. L., Liu, X. and Zhang, Y. Y. (2015). Concentration measurement of dilute pulverized fuel flow by Electrical Capacitance Tomography, *Instrum Sci Technol*, **43**(1), pp. 89-106.

- Wang, C., Zhang, J., Gao, W., Ding, H. and Wu, W. (2017). Cross-correlation focus method with an electrostatic sensor array for local particle velocity measurement in dilute gas–solid two-phase flow, *Meas Sci Technol*, **26**, pp. 1-10.
- Wang, L., Yan, Y., Wang, X., Wang, T., Duan, Q. and Zhang, W. (2018). Mass flow measurement of gas-liquid two-phase CO<sub>2</sub> in CCS transportation pipelines using Coriolis flowmeters, *Int J Greenh Gas Con*, **68**, pp. 269-275.
- Weber, J. M., Bobek, M. M., Breault, R. W., Mei, J. S. and Shadle, L. J. (2018). Investigation of core-annular flow in an industrial scale circulating fluidised bed riser with electrical capacitance volume tomography (ECVT), *Powder Technol*, **327**, pp. 524-535.
- Wen, Z., Ma, X. and Zuo, H. (2014). Characteristics analysis and experiment verification of electrostatic sensor for aero-engine exhaust gas monitoring, *Measurement*, **47**, pp. 633-644.
- Xiancheng, Q. and Yong, Y. (2012). Flow measurement of biomass and blended biomass fuels in pneumatic conveying pipelines using electrostatic sensor-arrays, *IEEE Trans Instrum Meas*, **61**(5), pp. 1343-1352.
- Xie, C. G., Plaskowski, A. and Beck, M. S. (1989). 8-electrode capacitance system for two component flow identification: Tomographic flow imaging, *IEE Proc-A*, **136**(4), pp. 173-183.
- Xie, C. G., Huang, S. M., Hoyle, B. S., Thorn, R., Lenn C., Snowden, D. M. S. and Beck, M. S. (1992). Electrical Capacitance Tomography for Flow Imaging: System Model for Development of Image Reconstruction Algorithms and Design of Primary Sensor, *IEE Proc G*, **139**(1), pp.89-98.
- Xie, C. G., Stott, A. L., Plaskowski, A. and Beck, M. S. (1990). Design of capacitance electrodes for concentration measurement of two-phase flow, *Meas Sci Technol*, **1**, pp. 65-78.
- Xu, C., Li, J. and Wang, S. (2012). A spatial filtering velocimeter for solid particle velocity measurement based on linear electrostatic sensor array, *Flow Meas Instrum*, **26**, pp. 68-78.
- Yan, Y., Byrne, B., Woodhead, S. and Coulthard, J. (1995). Velocity measurement of pneumatically conveyed solids using electrodynamic sensors, *Meas Sci Technol*, **6**(5), pp. 515.
- Yan, Y. and Ma, J. (2000). Measurement of particulate velocity under stack-flow conditions, *Meas Sci Technol*, **11**(1), pp. 59.
- Yan, H., Shao, F. and Wang, S. (1999). Simulation study of capacitance tomography sensors, *Proceedings of 1st World Congress on Industrial Process Tomography*, Buxton, UK, pp. 522-529.
- Yan, Y., Xie, Z., Krabicka, J. and Shao, J. (2010). Non-contact strip speed measurement using electrostatic sensors, In *Instrumentation and Measurement Technology Conference (I2MTC) 2010 IEEE*, pp. 1535-1538.

- Yang, C., Cui, Z., Xue, Q., Wang, H., Zhang, D. and Geng, Y. (2014). Application of a high speed ECT system to online monitoring of pneumatic conveying process, *Measurement*, **48**, pp. 29-42.
- Yang, W. Q. (1995). Hardware design of electrical capacitance tomography system, *Meas Sci Technol*, **7**(3), pp. 225-232.
- Yang, W. Q. (2010). Design of electrical capacitance tomography sensors, *Meas Sci Technol*, **21**(4), pp. 1-13.
- Yang, W. Q., Adam, M. S., Watson, R. and Beck, M. S. (1996). Monitoring water hammer by capacitance tomography, *Electron Lett*, **32**, pp. 1778–1779.
- Yang, W. Q. and Byars, M. (1999). An improved normalization for electrical capacitance tomography, *Proceedings of 1st World Congress on Industrial Process Tomography*, Buxton, UK, pp. 215-218.
- Yang, W. Q. and Peng, L. (2003). Image reconstruction algorithms for electrical capacitance tomography, *Meas Sci Technol*, **14**(1), pp. R1-R13.
- Yang, Y., Zhang, Q., Zi, C., Huang, Z., Zhang, W., Liao, Z., Wang, J., Yang, Y., Yan, Y. and Han, G. (2016). Monitoring of particle motions in gas-solid fluidized beds by electrostatic sensors, *Powder Technol*, **308**, pp.461-471.
- Yuan, J., Na, C., Lei, Q., Xiong, M., Guo, J. and Hu., Z. (2018). Coal use for power generation in China, *Resour Conserv Recycl*, **129**, pp. 443-453.
- Zainal-Mokhtar, K. and Mohamad-Saleh, J. (2013). An oil fraction neural sensor developed using Electrical Capacitance Tomography sensor data, *Sensor*, **13**(9), pp. 11385-11406.
- Zhang, J. (2002). *A study of an electrostatic flowmeter*, PhD Thesis, University of Teeside, UK.
- Zhang, J., Teixeira, A. R. and Jensen, K. F. (2018a). Automated measurements of gas-liquid mass transfer in micropacked bed reactors, *React Kinet Catal*, **64**(2), pp. 564-570.
- Zhang, W., Cheng, X., Hu, Y. and Yan, Y. (2018b). Measurement of moisture content in a fluidized bed dryer using an electrostatic sensor array, *Powder Technol*, **325**, pp. 49-57.
- Zhao, T., Takei, M., Masaki, K., Ogiso, R., Nakao, K. and Uchiura, A. (2007). Sensor design and image accuracy for application of capacitance CT to the petroleum refinery process, *Flow Meas Instrum*, **18**, pp. 268–276.
- Zhu, S., Lyu, Q., Zhu, J. and Liang, C. (in press). Experimental study on NOx emissions of pulverized bituminous coal combustion preheated by a circulating fluidized bed, *J Inst Energ*, <https://doi.org/10.1016/j.joei.2018.01.011>.